RESEARCH ARTICLE

Interspecific variation in bristle number on forewings of tiny insects does not influence clap-and-fling aerodynamics

Vishwa T. Kasoju[1], Daniel S. Moen[2], Mitchell P. Ford[1], Truc T. Ngo[1] and Arvind Santhanakrishnan[1],*

ABSTRACT

Miniature insects must overcome significant viscous resistance in order to fly. They typically possess wings with long bristles on the fringes and use a clap-and-fling mechanism to augment lift. These unique solutions to the extreme conditions of flight at tiny sizes (<2 mm body length) suggest that natural selection has optimized wing design for better aerodynamic performance. However, species vary in wingspan, number of bristles (n) and bristle gap (G) to diameter (D) ratio (G/D). How this variation relates to body length (BL) and its effects on aerodynamics remain unknown. We measured forewing images of 38 species of thrips and 21 species of fairyflies. Our phylogenetic comparative analyses showed that n and wingspan scaled positively and similarly with BL across both groups, whereas G/D decreased with BL, with a sharper decline in thrips. We next measured aerodynamic forces and visualized flow on physical models of bristled wings performing clap-and-fling kinematics at a chord-based Reynolds number of 10 using a dynamically scaled robotic platform. We examined the effects of dimensional (G, D, wingspan) and non-dimensional (n, G/D) geometric variables on dimensionless lift and drag. We found that: (1) increasing G reduced drag more than decreasing D; (2) changing n had minimal impact on lift generation; and (3) varying G/D minimally affected aerodynamic forces. These aerodynamic results suggest little pressure to functionally optimize n and G/D. Combined with the scaling relationships between wing variables and BL, much wing variation in tiny flying insects might be best explained by underlying shared growth factors.

KEY WORDS: Thrips, Fairyflies, Bristled wing morphology, Phylogenetic comparative analyses, Physical models, Weis-Fogh mechanism

INTRODUCTION

The wings of flying insects show tremendous diversity in shape, size and function. Curiously, the wings of several families of flight-capable insects smaller than fruit flies have independently evolved ptiloptery (Polilov, 2015; Sane, 2016), meaning wings with long setae at the fringes. Though their extremely small sizes (body length <2 mm) make visual observation difficult, tiny flying insects are not limited to just a few outlying examples. Rather, more than 5500 species of thrips (Thysanoptera; Morse and Hoddle, 2006), as well as several hundred species of bristle-winged wasps (Trichogrammatidae, Mymaridae, Mymarommatidae; Heraty et al.,

[1]School of Mechanical and Aerospace Engineering, Oklahoma State University, Stillwater, OK 74078-5016, USA. [2]Department of Integrative Biology, Oklahoma State University, Stillwater, OK 74078, USA.

*Author for correspondence (askrish@okstate.edu)

A.S., 0000-0003-1800-8361

2013), have been identified to date. Despite their importance as biological vectors of plant viruses and as invasive pests of commercially important plants (Ullman et al., 2002; Jones, 2005), we still understand little of the flight mechanics of tiny insects. Owing to the difficulty in acquiring free-flight recordings of tiny insects, several studies have used physical and computational modeling to examine the functional significance of wing bristles (Santhanakrishnan et al., 2014; Jones et al., 2016; Lee and Kim, 2017; Kasoju et al., 2018). While these studies have shown that having bristles aids flight at such small sizes, little is known about the extent of variation in bristled wing morphology among different species of tiny insects. Moreover, it remains unclear whether tiny insects experience selective pressure to optimize the mechanical design of their bristled wings, particularly given the extreme challenges of flight at miniature body sizes.

Pronounced viscous dissipation of kinetic energy occurs at wing length scales on the order of 1 mm, making it difficult for tiny insects to stay aloft. The relative importance of inertial to viscous forces in a fluid flow is characterized using the dimensionless Reynolds number ($Re=\rho VL/\mu$), where ρ and μ are the density and dynamic viscosity of the fluid medium, respectively, and V and L are characteristic velocity and length scales, respectively. The length scale has been examined based on wing chord (i.e. $L=c$; Re_c) and bristle diameter ($L=D$; Re_b), with Re_c on the order of 1 to 10 and Re_b ranging between 0.01 and 0.07 (Ellington, 1975; Kuethe, 1975; Santhanakrishnan et al., 2014; Jones et al., 2016). Despite the difficulty of sustaining flight at such low Re, entomological studies have reported active flight and dispersal of thrips (Morse and Hoddle, 2006; Rodriguez-Saona et al., 2010). Tiny insects use biomechanical adaptations to overcome the fluid dynamic challenges associated with flight at small scales. These insects operate their wings at near-maximum stroke amplitude using the 'clap-and-fling' mechanism, first observed by Weis-Fogh (1973) in *Encarsia formosa* (Hymenoptera). The use of clap-and-fling has been documented in other freely flying tiny insects, including *Thrips physapus* (Thysanoptera; Ellington, 1975) and *Muscidifurax raptor* (Hymenoptera; Miller and Peskin, 2009). Wing rotation during fling has been noted to augment lift via the generation of a leading edge vortex on the wings (Weis-Fogh, 1973, 1975; Lighthill, 1973; Spedding and Maxworthy, 1986; Dickinson et al., 1999; Birch et al., 2004; Miller and Peskin, 2005, 2009; Lehmann et al., 2005; Lehmann and Pick, 2007; Arora et al., 2014; Santhanakrishnan et al., 2018). However, the concomitant generation of large drag force at the start of fling undermines the advantage of clap-and-fling at Re_c relevant to tiny insect flight (Miller and Peskin, 2005; Arora et al., 2014). Previous studies have thus examined the flow structures and aerodynamic forces generated by bristled wings in comparison with solid wings (Sunada et al., 2002; Santhanakrishnan et al., 2014; Jones et al., 2016; Lee and Kim, 2017; Lee et al., 2018; Kasoju et al., 2018; Ford et al., 2019), showing that bristled areas on the wings can reduce the force required to fling the wings apart.

1

List of symbols and abbreviations

A	surface area of rectangular planform wing
A_B	area occupied by bristles of a bristled wing
A_M	area of solid membrane of a bristled wing
A_T	total wing area
BL	body length
c	wing chord
c_{ave}	average wing chord
$\bar{C}$	cycle-averaged force coefficient
C_D	drag coefficient
$\bar{C}_D$	cycle-averaged drag coefficient
$C_{D,max}$	peak drag coefficient
C_L	lift coefficient
$\bar{C}_L$	cycle-averaged lift coefficient
$C_{L,max}$	peak lift coefficient
CMOS	complementary metal-oxide-semiconductor
D	bristle diameter
F_T	tangential force on a wing
F_N	normal force on a wing
F_D	drag force
F_L	lift force
FOV	field of view
G	inter-bristle spacing (or gap)
G/D	inter-bristle gap to bristle diameter ratio
L_b	bristle length on either side of the solid membrane of a bristled wing
Le	leakiness
Le_{max}	maximum leakiness
LEV	leading edge vortex
n	number of bristles
PGLS	phylogenetic generalized least squares
PIV	particle image velocimetry
PLA	polylactic acid
PL-PIV	phase-locked PIV
Q	volumetric flow rate of fluid
$Q_{bristled}$	Q for bristled wing
$Q_{inviscid}$	volumetric flow rate leaked through the bristles under no viscous forces (inviscid flow)
Q_{solid}	Q for solid wing
$Q_{viscous}$	volumetric flow rate leaked through the bristles under viscous conditions
Re	Reynolds number
Re_b	Reynolds number based on bristle diameter
Re_c	Reynolds number based on wing chord
S	wingspan of a rectangular wing
S_{max}	maximum wingspan
t	instantaneous time
T	time duration for one cycle of clap-and-fling
TEV	trailing edge vortex
TR-PIV	time-resolved PIV
u	horizontal velocity along x-axis
U	instantaneous wing tip velocity
U_{rot}	instantaneous rotational velocity
U_{ST}	steady translational velocity
U_{tip}	wing tip velocity in the direction normal to the instantaneous wing position
U_{trans}	instantaneous translational velocity
VP	vertical plane
w	membrane width
α	instantaneous angle of the wing relative to the vertical
Γ	circulation of a vortex
Γ_{LEV}	circulation of the leading edge vortex
Γ_{TEV}	circulation of the trailing edge vortex
μ	dynamic viscosity of fluid
ν	kinematic viscosity of fluid
ρ	fluid density
λ	measure of phylogenetic signal
τ	dimensionless time
ω_z	z-component of vorticity

Despite this focus on modeling, morphological variation of bristled wing design in tiny flying insects is far less documented. Jones et al. (2016) examined the inter-bristle gap (G), bristle diameter (D) and wing area covered by bristles in the forewings of 23 species of fairyflies (Hymenoptera: Mymaridae and Mymarommatidae). With decreasing body length (BL), they found that G and D decreased and area occupied by bristles increased. Moreover, Ford et al. (2019) found that the percentage of solid membrane area (A_M) to total wing area (A_T) in the forewings of 25 species of thrips ranged from 14% to 27%, as compared with the percentage of A_M to A_T ranging from 11% to 88% in smaller-sized fairyflies examined by Jones et al. (2016). Yet interspecific variation of G, D, wingspan (S) and number of bristles (n), as well as their concomitant effects on clap-and-fling aerodynamics, are currently unknown.

Such variation in wing morphology across species may arise from many factors. Adaptation drives much interspecific variation (Futuyma and Kirkpatrick, 2017), and many studies have thus focused on the consequences of variation for optimal functional performance. For example, Ford et al. (2019) used physical models to test the aerodynamic consequences of variation in proportion of solid (i.e. compared with bristled) area on wings. They showed that lift-to-drag ratios were largest for bristled wing models with proportions similar to thrips forewings, suggesting that selection may maintain the small range of variation in thrips. Alternatively, variation among species may have little adaptive explanation (Gould and Lewontin, 1979). Contingent factors in evolution may cause distantly related groups to differ, even under the same selective pressures (Gould, 2002; Blount et al., 2018). Thus, high phylogenetic inertia may explain why species from differing clades differ in phenotype (Hansen and Orzack, 2005). Paradoxically, shared evolutionary history can also explain variation among more closely related species. Such species often share factors (e.g. developmental, genetic) that have similar effects on different traits; when one such trait varies among species, the other will likewise vary. For example, shared growth factors underlying different body parts can cause them to covary with body size. If closely related species differ in selection for body size, then they will similarly differ in traits that grow with body size during development. Strong scaling relationships (i.e. allometry) may indicate evolutionary history as a source of interspecific variation (Pélabon et al., 2014). Thus, accounting for phylogenetic relationships and estimating evolutionary inertia can also help explain variation among species.

In this study, we quantified variation in morphology across species of bristle-winged insects and addressed the factors potentially driving this variation. We first measured wing morphology from 59 species of thrips and fairyflies. We then conducted phylogenetic regressions of key variables on body length and we quantified evolutionary inertia. Using the morphological data as a guide for biologically relevant variation, we then fabricated physical bristled wing models varying in G, D, maximum wingspan (S_{max}) and n. These physical models were comparatively tested using a dynamically scaled robotic platform mimicking the portion of clap-and-fling kinematics where wing–wing interaction occurs. Aerodynamic force measurements and flow field visualization were conducted to identify the functional significance of the above bristled wing design variables. Because of the high variation in n and G/D despite the extreme aerodynamic demands of flight at small size, we hypothesized that at Re relevant to tiny insect flight, dimensionless aerodynamic forces generated by clap-and-fling would be minimally impacted by variation in n and G/D within their biological ranges. If true, tiny flying insects may not experience

selective pressure to further functionally optimize the mechanical design of their bristled wings.

MATERIALS AND METHODS
Forewing morphology
We measured average BL, A_T, S_{max}, n, G and D from published forewing images of thrips and fairyflies, whose size ranged from 0.1 to 2 mm in BL. In the Supplementary Materials and Methods, we detail our criteria for choosing published forewing images for measurement. Based on these criteria, we selected forewing images of 16 thrips species for measuring S_{max}, A_T and n, and of 22 different thrips species for measuring G and D (Mound and Reynaud, 2005; Mound, 2009; Zhang et al., 2010; Riley et al., 2011; Cavalleri and Mound, 2012, 2014; Ng and Mound, 2015; Masumoto et al., 2013; Minaei and Aleosfoor, 2013; Zamar et al., 2013; Dang et al., 2014; Cavalleri et al., 2016; Lima and Mound, 2016a,b; Mound and Tree, 2016; Wang and Tong, 2016; Goldaracena and Hance, 2017; PaDIL: http://www.padil.gov.au). The thrips species considered here encompassed three different taxonomic families. In addition, we selected 21 fairyfly species for measuring S_{max}, A_T and n (Huber et al., 2006, 2008; Huber and Baquero, 2007; Lin et al., 2007; Huber and Noyes, 2013), largely overlapping those of Jones et al. (2016), who presented data on G and D for 23 species.

We measured bristled wing morphological variables from these images using ImageJ software (Schneider et al., 2012). S_{max} was defined to be the distance from the center of the wing root to the tip of the bristles, following Fig. 1A. Average wing chord (c_{ave}) was calculated by measuring A_T using the same procedure as in Jones et al. (2016) and Ford et al. (2019), then dividing A_T by S_{max}. G/D ratio was calculated from the measurements of G and D in the forewing images. BL measurements were made either from images (where available) or from the text of the article containing the image. A full list of species, corresponding measurements and publication sources of the original images is provided as Appendix S1 in Figshare (https://doi.org/10.6084/m9.figshare.14478108.v1).

Morphological analysis
We accounted for shared evolutionary history among species in our regressions by using phylogenetic generalized least squares (PGLS; Martins and Hansen, 1997). Regressions were fit with the maximum-likelihood value of λ (Pagel, 1999), the phylogenetic signal of regression residuals. This procedure best balances species similarity owing to shared history and shared adaptation (Hansen and Orzack, 2005), which improves statistical inference (Revell, 2010). Moreover, λ can be used as a metric of the role of evolutionary history in a fitted relationship (Hansen and Orzack, 2005).

Phylogenetic data for our study species were scarce. Only nine of our 59 species of thrips and fairyflies were included in published phylogenies, and these nine were scattered across published trees (Munro et al., 2011; Buckman et al., 2013; Lima and Mound, 2016a, b; Pereyra et al., 2019). Thus, we simulated many possible phylogenies for our study species and conducted comparative analyses across these trees. This procedure allowed for both integration over phylogenetic uncertainty (Martins, 1996) and
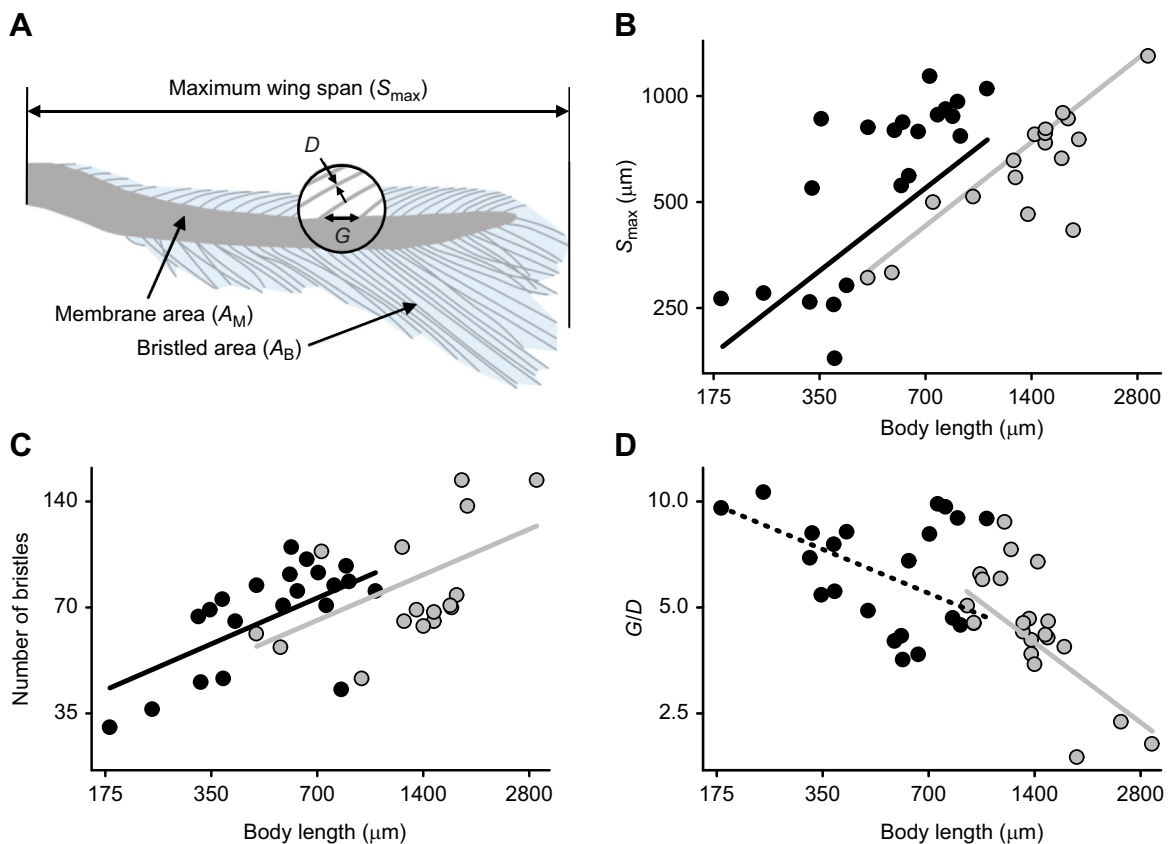

Fig. 1. Morphological measurements and scaling relationships with body length (BL) in thrips and fairyflies. All scatterplots have data plotted in original units on a logged scale. (A) Forewing of *Thrips setosus* (BL=1400 μm) redrawn from Riley et al. (2011), with bristled area (A_B), membrane area (A_M), maximum wingspan (S_{max}), inter-bristle gap (G) and bristle diameter (D) indicated. (B) S_{max} as a function of BL. (C) Number of bristles as a function of BL. (D) G/D as a function of BL. Gray lines and points indicate thrips, while black indicates fairyflies. Solid lines in the same plot indicate that slopes were the same in the most-supported models, while dotted and solid lines indicate statistical support for differing slopes (Table 1, Table S2).

assessment of the sensitivity of our results to any specific potential phylogeny (Losos, 1994). Herein, we briefly summarize our procedure for simulating phylogenies. We refer readers to the Supplementary Materials and Methods for detailed simulation methods, justification and discussion of why phylogenetic regressions should be robust to variation or error in phylogeny.

We constrained our simulated trees to fit current taxonomic knowledge, as adding some phylogenetic structure increases accuracy over completely random approaches (Housworth and Martins, 2001; Martins, 1996; Martins and Housworth, 2002; Symonds, 2002). This meant, for example, that all species of a given genus were each other's closest relatives in every simulated tree. For thrips, taxonomic information was extracted from the comprehensive Thrips Wiki (https://thrips.info/wiki/; accessed 15 March 2021). Fairyflies are likely a polyphyletic group of two families in two superfamilies of wasps (Mymarommatoidea: Mymarommatidae and Chalcidoidea: Myrmaridae; Huber, 1986; Davis et al., 2010; Munro et al., 2011); in simulations we assumed these two families to be each other's sister taxon. Genera for these two families were extracted from taxonomic accounts (Gibson et al., 2007; Huber, 2005, 2017; Lin et al., 2007; Poinar and Huber, 2011). Phylogenies were simulated in the package phytools v.0.7-70 (Revell, 2012) in R v.4.0.2 (https://www.r-project.org/). We simulated 10,000 trees, then pruned each tree to only include the species for which we had phenotypic data, which varied based on the response variable. All tree simulation R code, taxonomic information and resulting trees are included in Figshare as Appendices S2–S4 (https://doi.org/10.6084/m9.figshare.14478108.v1).

Regression analyses were conducted on logged variables, as is standard in body-size scaling analyses (Voje and Hansen, 2013; Pélabon et al., 2014; Glazier, 2021). For each simulated tree, we compared four nested models: (1) a null model with only an intercept; (2) a simple model of regression in which both thrips and fairyflies shared all parameters; (3) a model in which both groups shared a scaling slope but had different intercepts; and (4) a full model in which both groups differed in slope and intercept. These models thus allowed us to estimate scaling relationships between variables and ask whether such relationships differed in thrips and fairyflies (Gartner et al., 2010; Moen et al., 2016). All regressions were estimated in the package phylolm v.2.6.2 (Ho and Ané, 2014). We compared models for each tree with the corrected Akaike's information criterion (AICc) and its associated weights (Burnham and Anderson, 2002). We used the model weights to calculate model-averaged regression parameters, adjusted R^2 and λ values (Burnham and Anderson, 2002; Posada and Buckley, 2004). We then averaged these values across trees, as well as the AICc values and model weights. Assuming that each randomly resolved tree is equally likely, such means represent values integrated over phylogenetic uncertainty (Martins, 1996). We also calculated the 95% confidence intervals of slopes, accounting for both estimation and phylogenetic uncertainty (Martins, 1996). Finally, we calculated the proportion of trees in which a scaling model (i.e. models 2–4) had the highest weight. This proportion reflected the effect of phylogenetic structure on finding a non-zero scaling relationship (Losos, 1994).

Variation in wingspan, bristle number and G/D at different body lengths motivated our subsequent physical model experiments. However, we designed these models at a chord-based Re, rather than body length. Moreover, our experiments held two variables constant (e.g. wingspan and bristle number) while varying a third (e.g. G/D). Thus, we also examined PGLS correlations between these variables, likewise calculating means across the simulated phylogenies, as above. We estimated these correlations using custom R code from

Moen et al. (2013), following Rohlf (2006). All R code for regression and correlation analyses, as well as for producing the resulting figures, is provided in Appendices S5–S6 on Figshare (https://doi.org/10.6084/m9.figshare.14478108.v1).

Simplified wing models

Our forewing morphological measurements in thrips and fairyflies showed large variation in n (32 to 161). n for a bristled wing of rectangular planform (Fig. 2A) with constant w, G and D can be calculated using the following equation:

$$n = \frac{2S}{G + D}, \tag{1}$$

where n represents the total number of bristles on both sides of a solid membrane. The reason for choosing a rectangular wing planform is because the changes in wing shape are not expected to affect the trend of aerodynamic force generation in time during clap-and-fling, as seen when comparing the lift and drag coefficients of rectangular bristled wing pairs (Kasoju et al., 2018) with those of approximated elliptical bristled wing pairs (Ford et al., 2019) at chord-based Reynolds number (Re_c) of 10. We designed and fabricated 14 pairs of scaled-up, simplified (rectangular planform) physical wing models to examine effects of changing G, D and S (Table S1). In addition, nine wing pairs were used to examine the variation in non-dimensional geometric variables: n and G/D (Table S1). Note that we rounded n down to a whole number in the physical models. As our wing models were scaled up, we were not able to match G, D and S values to be in the range of tiny insects. To achieve geometric similarity, we maintained the relevant non-dimensional geometric variables (n and G/D) to be within their corresponding biological ranges in all the physical models.

The bristled wings tested in this study were simplified to rectangular shape with constant wing chord (c in Fig. 2A) to minimize variability in confinement effects along the wingspan from the tank walls. The percentage of A_M/A_T in all the models was maintained at 15%, which is in the range of A_M/A_T of thrips and fairyflies (Ford et al., 2019). Bristle length (L_b, see Fig. 2A) and w were maintained as constants on either side of the membrane for all 23 wing models tested. The values of constants c, L_b and w are provided in Table S1.

Scaled-up physical models were used in this study to examine the roles of bristled wing geometric variables on clap-and-fling aerodynamics at Re_c=10. We used this approach to overcome the difficulty of resolving the flow around and through a bristled wing on the scale of 1 mm length. As we did not match the values of dimensional geometric variables to those of real insects, we used geometric similarity to match non-dimensional variables (n, G/D) in all the physical models to be in the range of tiny insects. As n depends on G, D and S per Eqn 1, the choices of non-dimensional variables include n, G/D, G/S and D/S. We chose G/D to match Jones et al. (2016). In addition, to understand the isolated role of each dimensional variable, we tested scaled-up models varying in G, D and S. For each condition, we maintained the two other dimensional variables as constants and also matched the non-dimensional variables (n, G/D) to be within their biologically relevant ranges identified from morphological analysis. For details on the fabrication details of bristled wing models, refer to the Supplementary Materials and Methods.

Dynamically scaled robotic platform
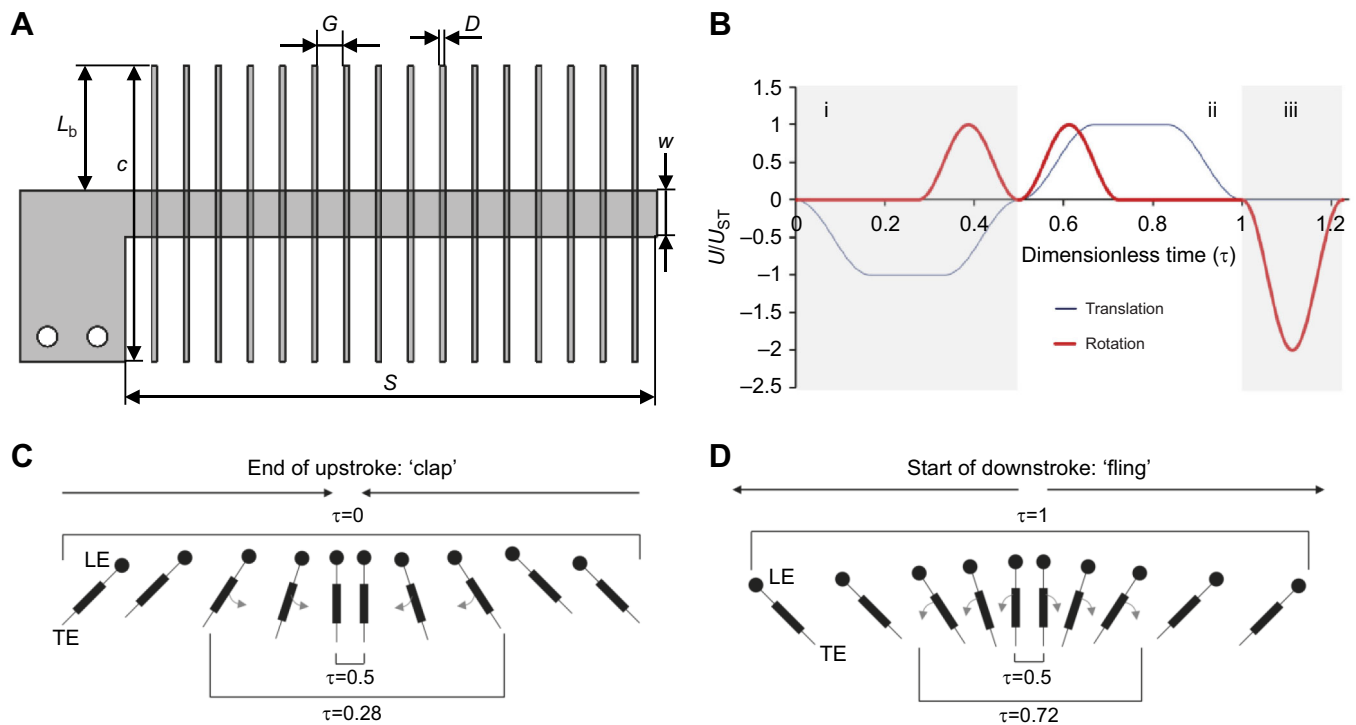The dynamically scaled robotic platform used in this study (Fig. 3A,B) has been described in previous studies

Fig. 2. Physical bristled wing model and kinematics. (A) Diagram of the simplified bristled wing model with rectangular planform (L_b, bristle length; w, membrane width; c, wing chord; S, wingspan). See Table 1 for the complete list of models tested. (B) Prescribed motion profile of a single wing, based on kinematics developed by Miller and Peskin (2005). Dimensionless velocity (U/U_{ST}) is shown as a function of dimensionless time (τ). The wing motion consisted of rotation (thick line) and translation (thin line) along three regions: (i) clap ($\tau=0$–0.5); (ii) fling ($\tau=0.5$–1); and (iii) 90 deg wing rotation ($\tau=1$–1.2) to position the wing for the start of the next cycle. During both clap and fling, wing translation was prescribed to occur throughout the wing rotation (100% overlap). The motion profiles prescribed to the other wing was identical in magnitude but opposite in sign, so that the wings would travel in opposite directions. Forces and PIV data were acquired from start of clap to the end of fling. Diagrammatic representation of wing motion during clap (C) and fling (D), where the sectional view along the wingspan is shown. $\tau=0$, 0.28 and 0.5 correspond to start of clap (wings translating toward each other), start of wing rotation and end of clap, respectively. $\tau=0.5$, 0.72 and 1 correspond to start of fling with wings rotating and translating apart, end of wing rotation and end of fling, respectively. U, instantaneous wing tip velocity; U_{ST}, steady translational velocity; LE, leading edge; TE, trailing edge.
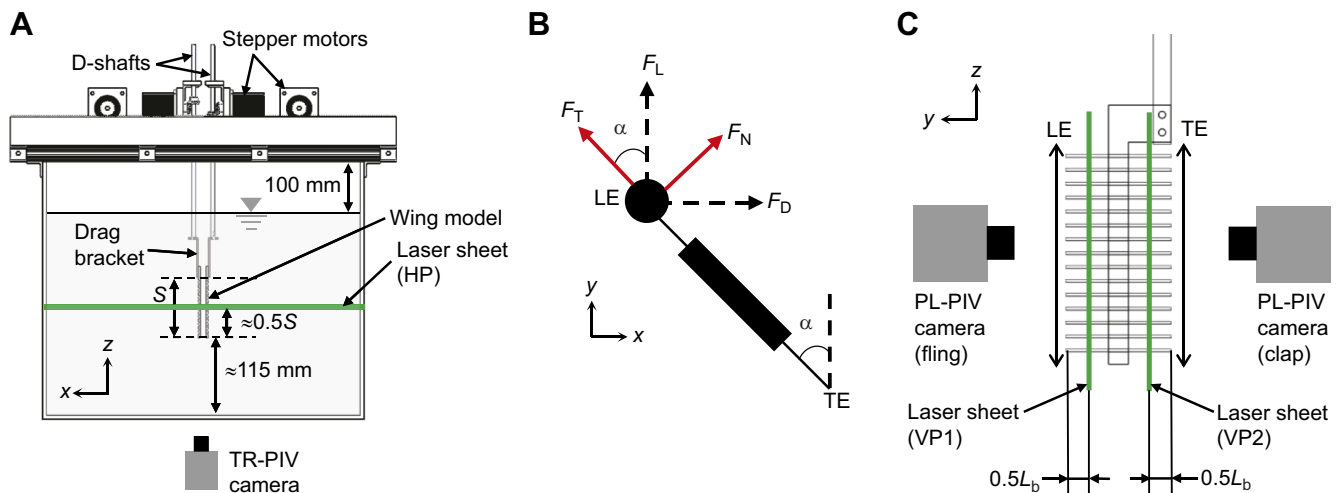

Fig. 3. Robotic platform and experimental setup. (A) Front view of the robotic platform with bristled wings attached using custom L-brackets with strain gauges to measure the forces generated by a wing during clap and fling phases. The tank measured 510×510 mm in cross-section and 410 mm in height. Two-dimensional TR-PIV was used to visualize the chordwise flow field generated during clap and fling phases, where raw images were acquired using a high-speed camera and illumination was provided with a horizontally oriented laser sheet (horizontal plane, HP) located approximately at mid-span (0.5S). (B) Sectional view along spanwise direction for a single bristled wing with directions of measured tangential (F_T) and normal forces (F_N) on a wing during rotation by angle α with respect to the vertical. Lift (F_L) and drag (F_D) forces were measured using a lift and drag bracket, respectively, by taking components of F_T and F_N in the vertical (F_L) and horizontal (F_D) directions. (C) Two-dimensional PL-PIV was used to measure the inter-bristle flow for six equally spaced time points during clap ($\tau\sim0.13$ to $\tau\sim0.44$) using a vertically oriented laser sheet (vertical plane 1, VP1) and seven equally spaced time points during fling ($\tau\sim0.63$ to $\tau\sim0.94$) at laser sheet labeled VP2. Both VP1 and VP2 were located at 0.5L_b from the LE and TE, respectively. x,y,z are fixed coordinate definitions.

(Kasoju et al., 2018; Ford et al., 2019) and experimentally validated against results in Sunada et al. (2002) corresponding to a single wing in translation at varying angles of attack (in Kasoju et al., 2018). For more details on the robotic platform and justification of our forewing approach, refer to the Supplementary Materials and Methods.

Kinematics

Free-flight recordings adequate for characterizing instantaneous wing kinematics are unavailable for most species of tiny insects. Thus, we used a modified version of 2D clap-and-fling kinematics developed by Miller and Peskin (2005). The simplified kinematics used here do not capture: (1) 3D flapping translation during the downstroke and upstroke, and (2) wing rotation at the end of the downstroke ('supination'). In real insects, the flapping cycle includes the combination of wing revolution (which we referred to as '3D flapping translation' following terminology in Sane, 2003), wing rotation and elevation with respect to the root of the wing. In our study, the wings rotated and translated along a horizontal line with no change in elevation or stroke angle (Fig. 3C,D). 'Wing rotation at the end of downstroke' refers to the ventral stroke reversal (supination) at the end of downstroke that is observed in 3D flapping flight. In this study, a 'stroke cycle' is defined as a clap stroke and fling stroke (the latter corresponding to pronation or dorsal stroke reversal) and does not include the ventral stroke reversal occurring towards the end of downstroke. Similar or modified forms of these kinematics have been used in several other studies (Miller and Peskin, 2004, 2009; Santhanakrishnan et al., 2014; Arora et al., 2014; Jones et al., 2016; Kasoju et al., 2018; Ford et al., 2019; Kasoju and Santhanakrishnan, 2021). Fig. 2B shows the motion profiles prescribed for a single wing, where dimensionless velocity (instantaneous wing tip velocity U divided by steady translational velocity U_{ST}) is provided as a function of dimensionless time (τ) during rotational and translational motion. τ was defined as $\tau = t/T$, where t represents instantaneous time and T represents time taken to complete one cycle of clap-and-fling. The motion profile for the other wing was identical in magnitude but opposite in sign, so that the wings would travel in opposite directions. Both wings moved along a straight line (no change in elevation and stroke angles). Schematic diagrams of the clap phase (Fig. 2C) and fling phase (Fig. 2D) are provided to show the direction of motion and wing position at the start and end of each portion of each half-stroke. The wings were programmed to start from an initial position corresponding to the start of the clap phase, and this was followed by the wings moving toward each other until the start of the fling phase, after which the wings moved apart from each other. The distance between the wings at the end of the clap phase was set to 10% of chord length, which we justify in the Supplementary Materials and Methods. In addition, the wingbeat kinematics are undescribed for most species of tiny insects and are likely variable across species (Lyu et al., 2019). For the present study, we prescribed 100% overlap between rotation and translation during both clap and fling, meaning that the wings translated during the entire rotational time. This was because previous studies (Arora et al., 2014; Kasoju and Santhanakrishnan, 2021) have shown that high overlap between rotational and translational motions significantly increases the aerodynamic forces (both lift and drag).

Test conditions

Each wing model used in this study was tested at a chord-based Reynolds number of 10 ($Re_c=10$). The kinematic viscosity ($\nu = \mu/\rho$) of the 99% glycerin solution in which wing models were tested was measured using a Cannon-Fenske routine viscometer (size 400,

Cannon Instrument Company, State College, PA, USA) to be 860 mm^2 s^{-1} at room temperature. The chord-based Reynolds number was defined using the equation:

$$Re_c = \frac{\rho U_{ST} c}{\mu} = \frac{U_{ST} c}{\nu}, \qquad (2)$$

which we used to solve for U_{ST} at $Re_c=10$. Time-varying rotational and translational velocities were generated from the solved U_{ST} value using the equations in Miller and Peskin (2005). The complete duration of a clap-and-fling cycle (T) was 2220 ms. As c was invariant across all wing models (Table S1), Re_c was constant for all wing models tested using the same motion profile. Keeping Re_c constant, we varied Re_b to ensure that the flow through the bristles of a model would be on the same order of magnitude as those of real insects. Moreover, as we tested a range of other variables in this study (up to five, comprising G, D, n, S, G/D), we hesitated to add yet more variation in terms of Re_c.

Force measurements

Similar to Kasoju et al. (2018) and Ford et al. (2019), force measurements were performed using L-brackets with strain gauges mounted in half-bridge configuration (drag bracket shown in Fig. 3A). The strain gauge conditioner continuously measured the force as voltage, and a data acquisition board (NI USB-6210, National Instruments, Austin, TX, USA) synchronously acquired the raw voltage data and angular position of the wings once a custom LabVIEW (National Instruments) program triggered the recording at the start of a cycle. Force data and angular position of the wings were acquired for complete duration of clap-and-fling motion ($\tau=0$ to 1) at a sample rate of 10 kHz. We used the same processing procedures as in Kasoju et al. (2018), briefly summarized here. The voltage signal was recorded prior to the start of motion for a baseline offset. In this study, a particular experimental test run consisted of: (1) upstroke (clap phase), where wings move towards each other; (2) downstroke (fling phase), where wings moved apart from each other; and (3) stroke reversal at the end of downstroke for positioning the wing to start the upstroke for the next run. We paused for 30 s at the end of each run (after stroke reversal at the end of downstroke) before starting the subsequent run and acquiring the force data, which we justify in the Supplementary Materials and Methods. We acquired the force data for 30 stroke cycles (during clap stroke and fling stroke). The next step was to filter the raw voltage data in MATLAB (The MathWorks Inc., Natick, MA, USA) using a third-order low-pass Butterworth filter with a cut-off frequency of 24 Hz. The baseline offset was averaged in time and subtracted from the filtered voltage data. The lift and drag brackets were calibrated manually, and the calibration was applied to the filtered voltage data obtained from the previous step to calculate forces. The forces that were calculated represent tangential (F_T) and normal (F_N) forces (Fig. 3B). Lift force (F_L) is defined as the force acting in the vertical direction (y-axis; Fig. 3B) and drag force (F_D) is defined as the force acting in the direction opposite to wing motion (positive or negative x-axis depending on the wing motion). Dimensionless lift coefficient (C_L) and drag coefficient (C_D) were calculated using the following relationships:

$$C_L = \frac{F_L}{(1/2)\rho U_{ST}^2 A} = \frac{F_T \cos\alpha + F_N \sin\alpha}{(1/2)\rho U_{ST}^2 A}, \qquad (3)$$

$$C_D = \frac{F_D}{(1/2)\rho U_{ST}^2 A} = \frac{F_N \cos\alpha + F_T \sin\alpha}{(1/2)\rho U_{ST}^2 A}, \qquad (4)$$

where F_L and F_D are the lift and drag forces (in Newtons), respectively, α is the angular position of the wing relative to the vertical, recorded from the integrated encoder of the rotational stepper motor, ρ is the fluid density (measured to be 1260 kg m^{-3}), and A is the surface area of the rectangular planform of a wing ($A=Sc$). The force coefficients were phase-averaged across all cycles to obtain time-variation of instantaneous force coefficients within a cycle. In addition, cycle-averaged force coefficients ($\overline{C}_L$, $\overline{C}_D$) were calculated across 30 cycles. The design of lift and drag L-brackets and validation of the methodology can be found in Kasoju et al. (2018). Note that all forces were only recorded on a single wing, with the assumption that forces generated by the other wing of a wing pair were equal in magnitude, as the motion was symmetric for both wings of a wing pair.

Particle image velocimetry

Two-dimensional time-resolved particle image velocimetry (2D TR-PIV) measurements were conducted to characterize the flow generated during clap-and-fling motion by bristled wing pairs along the chordwise plane (data acquired along a horizontal plane shown in Fig. 3A). Two-dimensional TR-PIV based two-component velocity vector fields were also used to determine the strength (i.e. circulation) of the leading edge vortex (LEV) and the trailing edge vortex (TEV). Two-dimensional phase-locked PIV (2D PL-PIV) measurements were conducted to characterize flow leaked along the span of bristled wings (data acquired along two vertical planes shown in Fig. 3C). For more details on validation of 2D flow simplification, the experimental arrangements and processing steps used for 2D TR-PIV and 2D PL-PIV measurements, refer to the Supplementary Materials and Methods.

The processed TR-PIV images were phase-averaged over five cycles, and 2D velocity components and their positions were exported for calculating circulation (Γ) of the LEV and TEV. Γ was calculated for eight equally spaced time points in both clap (from τ=0.05 to 0.4; increments of 5% of τ) and fling (from τ=0.55 to 0.9; increments of 5% of τ). Γ was calculated from the following equation using a custom MATLAB script:

$$\Gamma = \iint \omega_z \mathrm{d}x\mathrm{d}y, \tag{5}$$

where ω_z represents the out-of-plane (i.e. z) component of vorticity at leading or trailing edge, calculated from exported velocity vectors similar to Ford et al. (2019). Integrating over dx and dy represents the area of the vorticity region selected for either the LEV or TEV. For more details on circulation calculation (Samaee et al., 2020), refer to the Supplementary Materials and Methods.

Cheer and Koehl (1987) proposed the use of a non-dimensional quantity called leakiness (Le) to characterize the amount of fluid leaking through bristled appendages. Le is defined as:

$$Le = \frac{Q_{\mathrm{viscous}}}{Q_{\mathrm{inviscid}}}, \tag{6}$$

where Q_{viscous} represents the volumetric flow rate leaked through the bristles in the direction opposite to appendage motion under viscous conditions, and Q_{inviscid} represents the same flow rate under no viscous forces (inviscid flow). Similar to Kasoju et al. (2018), we calculated the inviscid (or ideal) volumetric flow rate leaked through the bristles of a wing as:

$$Q_{\mathrm{inviscid}} = \left(S - \frac{nD}{2}\right)U_{\mathrm{tip}}, \tag{7}$$

where U_{tip} represents wing tip velocity in the direction normal to the instantaneous wing position, defined as:

$$U_{\mathrm{tip}} = U_{\mathrm{rot}}\cos\alpha + U_{\mathrm{trans}}, \tag{8}$$

where U_{trans} and U_{rot} represent instantaneous translational and rotational velocities, respectively, and α represents instantaneous angle of a single wing relative to the vertical (Fig. 3B). U_{rot} was calculated as the product of the wing chord (c) and angular velocity of the wing (ω_{rot}), as in Kasoju et al. (2018).

Q_{viscous} was calculated from 2D PL-PIV velocity field data as the difference in volumetric flow rates of a solid (non-bristled) wing (denoted herein by Q_{solid}) and the bristled wing under consideration, using the same steps as in Kasoju et al. (2018). We briefly summarize those steps here. Two-dimensional PL-PIV measurements were acquired on a solid wing model of the same c and S as that of the bristled wing under consideration, using identical motion profiles for both solid and bristled wings and at the same time points or 'phase-locked' positions. Horizontal velocity was extracted for the entire length of wingspan along a line l that was oriented parallel to the wingspan and located downstream of the wing (i.e. in the direction of wing motion) at an x-axis distance of approximately 5% chord length from the rightmost edge of the wing surface when viewing the wing along the x–z plane. The horizontal component of the 2D PL-PIV velocity fields was in the direction normal to the wing, i.e. velocity component in the direction of wing motion. These velocity profiles were extracted for every wing model tested, at six time points in clap and seven time points in fling. The viscous volumetric flow rate in the direction opposite to the wing motion (i.e. leaky flow) was calculated using the equation $Q_{\mathrm{viscous}}=Q_{\mathrm{solid}}-Q_{\mathrm{bristled}}$. Volumetric flow rates (per unit width) for both solid and bristled wings about line l was calculated by the line integral of the horizontal velocity using the equation below (in a custom MATLAB script):

$$Q_{\mathrm{wing}} = \int_l u\mathrm{d}z, \tag{9}$$

where u is horizontal velocity along the x-axis.

In some cases, it may be possible to directly estimate the reverse (i.e. leaky) viscous volumetric flow rate in the direction opposite to bristled wing motion from the 2D PL-PIV data. However, we were not able to calculate this flow rate directly because high-magnification images would be needed to resolve flow through inter-bristle gaps (i.e. on the order of a few millimeters). This conflicted with our desire to use lower magnification in order to resolve flow across the entire wingspan (i.e. 10× greater than G) for calculating Q_{viscous} across a bristled wing.

RESULTS

Forewing morphological analysis

Most variables showed considerable diversity across species. In thrips, S_{max} ranged from 305 to 1301 µm and bristle number (n) ranged from 44 to 161 (Fig. 1B,C). In fairyflies, S_{max} ranged from 180 to 1140 µm and n ranged from 32 to 104 (Fig. 1B,C). S_{max} increased with body length with negative allometry, meaning that larger individuals had relatively shorter wings than smaller individuals (Fig. 1B, Table 1). Most model weight across phylogenies indicated support for a model with the same slope and intercept for thrips and fairyflies (Table S2). n increased with body length similarly in both groups (Fig. 1C, Table 1), though there was nearly equivalent support for similar versus differing intercepts in the groups (Table S2). The latter meant more bristles at the same body length in fairyflies (Fig. 1C). In both S_{max} and n, however, we found that AICc model

Table 1. Results of regressions of wing parameters on body length

Trait	Optimal model	b_{Thrips}	$b_{\text{Fairyflies}}$	R^2_{adj}	λ	Prop$_{\text{phylo}}$
Wingspan (S_{max})	Same slope, intercept	0.769 (0.577, 0.962)	0.769 (0.577, 0.962)	0.672	0.852	1
Bristle number (n)	Same slope, intercept	0.434 (0.232, 637)	0.434 (0.232, 637)	0.350	0.005	1
G/D	Full	−0.760 (−1.160, −0.360)	−0.418 (−0.819, −0.018)	0.376	0.445	1

All analyses were performed on logged variables. 'Optimal model' indicates the model that had the highest mean weight across simulated phylogenies (Table S2). Most values indicate mean values across simulated phylogenies. b_{Thrips} and $b_{\text{Fairyflies}}$ indicate mean slope estimates for each group with 95% confidence intervals in parentheses. R^2_{adj} is the mean adjusted R^2. λ is the mean phylogenetic signal of regression residuals; a value of 0 indicates that species similarity in residuals is independent of phylogeny, whereas a value of 1.0 indicates that similarity is directly proportional to shared evolutionary history (Freckleton et al., 2002). Prop$_{\text{phylo}}$ is the the proportion of simulated phylogenies in which a scaling model (models 2–4) had the highest AICc weight. G/D, inter-bristle gap to bristle diameter ratio.

weight was concentrated on the two models with the same slopes for the two groups, which suggests similar scaling relationships. In contrast, while the inter-bristle gap to bristle diameter ratio (G/D) decreased with body length across both groups (Fig. 1D), the model with the most weight had a different slope and intercept for the two groups (Table S2). G/D more strongly decreased with increasing body length for the larger-sized thrips species (Fig. 1D, Table 1). The model in which both groups shared a slope and intercept also showed high statistical support across trees (Table S2). Regardless of the optimal model, these results mean that larger animals have more tightly packed bristles, with less leakage. Phylogenetic signal (λ) was close to 1 in S_{max} (i.e. residual species similarity reflects phylogeny), nearly 0 in n (i.e. similarity is independent of phylogeny) and intermediate in G/D.

Overall, our results suggest that both groups follow shared trends in bristle variables with BL across bristle-winged insects. Yet only BL strongly predicted S_{max}, with R^2_{adj} almost two times lower for both n and G/D (Table 1). These latter results made us predict that variation in these latter two variables would have less aerodynamic consequences than S_{max}, motivating our robotic model experiments. Given weak correlations among S_{max}, n and G/D (Table S3, Fig. S1), we probed the effect of varying each of these variables while holding the other two constant.

Force measurements

For all the wing models tested, C_{D} and C_{L} were observed to follow the same trends over time during both clap and fling (Fig. 4A,B). Peak C_{D} occurred during fling ($\tau\sim0.6$) in all wing models (Fig. 4A). This time point corresponds to the end of rotational acceleration and translational acceleration (Fig. 2B), such that the wing pair would experience larger viscous resistance. C_{D} was found to drop after $\tau\sim0.6$ until the wing rotation ended ($\tau\sim0.73$) for all the wing models (Fig. 4A). Just before the C_{D} reached the negative value at the end of fling where the wings decelerate, we observed C_{D} to plateau from $\tau\sim0.73$ to 0.84 (Fig. 4A). This time corresponds to steady translational motion of the wings (Fig. 2B), where the wings translate with constant velocity at 45 deg angle of attack. Most of the drag during a cycle was generated in fling. Temporal variation of C_{D} was lower during clap half-stroke ($\tau=0$–0.5) as compared with fling (Fig. 4A).

Three positive C_{L} spikes were observed in all wing models (Fig. 4B): (1) $\tau\sim0.6$ in fling, similar to that of peak C_{D}; (2) start of clap ($\tau\sim0.16$); and (3) end of clap ($\tau\sim0.38$). $\tau\sim0.16$ corresponds to the end of translational acceleration at a 45 deg angle of attack and $\tau\sim0.38$ corresponds to the end of rotational acceleration during clap (Fig. 2B). Peak C_{L} occurred during fling for all wing models. Unlike for drag force, both clap and fling half-strokes contributed almost equally to lift generation.

Both C_{D} and C_{L} decreased with increasing G and decreasing D (Fig. 4i,ii). Increasing S increased both C_{D} and C_{L} (Fig. 4iii). When increasing n for constant G/D, both C_{D} and C_{L} were found to increase (Fig. 4iv), particularly at the beginning of the fling phase.

In contrast, increasing G/D for constant n decreased both C_{D} and C_{L} (Fig. 4v). Across all the wing models tested, we observed noticeable negative lift towards the end of fling. This is due to the wings not coming to complete rest and performing stroke reversal to position the wings for clap for the next cycle.

Cycle-averaged force coefficients ($\overline{C}$) were used to examine how each geometric variable impacted aerodynamic forces in a complete cycle (Figs 5 and 6). Individually increasing G and D showed little to no variation in $\overline{C}_{\text{L}}$ when considering the standard deviations (Fig. 5A,B). $\overline{C}_{\text{D}}$ decreased with increasing G and showed little to no variation with increasing D (Fig. 5A,B). Both $\overline{C}_{\text{L}}$ and $\overline{C}_{\text{D}}$ increased with increasing S from intermediate to large values of S (Fig. 5C). $\overline{C}_{\text{D}}$ increased with increasing n (Fig. 6A). $\overline{C}_{\text{L}}$ increased with n, most notably at $n>88$, though it plateaued between some consecutive values (Fig. 6A). Increasing G/D showed little to no variation in $\overline{C}_{\text{L}}$ and $\overline{C}_{\text{D}}$ when considering the standard deviations (Fig. 6B), though extreme values of G/D slightly differed.

Inter-bristle flow characteristics

Spanwise distribution of horizontal velocity (u) was examined near the instant of peak C_{D} ($\tau\sim0.63$) from 2D PL-PIV velocity fields (Fig. 7A). Looking at the extremes of each test condition, u increased with: (1) decreasing G; (2) increasing D; (3) increasing S; (4) increasing n; and (5) decreasing G/D. This reveals how each variable (i.e. G, D, S, n, G/D) differentially affects flow through a bristled wing. Similar to C_{D}, Le was observed to peak during fling. During the fling half-stroke, Le peaked either at $\tau\sim0.56$ or $\tau\sim0.63$ for all wing models (Fig. 7B) where the wings were near the end of rotational acceleration (Fig. 2B). Similarly, wing deceleration during fling from $\tau\sim0.69$ to $\tau\sim0.88$ resulted in a drop in Le (Fig. 7B). During steady wing translation from $\tau\sim0.75$ to $\tau\sim0.82$, Le was found to almost plateau in all wing models.

Le was larger in early clap ($\tau\sim12.5$) right after the wing pair started from rest, with minimal time for boundary layers around each bristle to be well developed. Thereafter, Le decreased with increasing clap duration until $\tau\sim0.38$, corresponding to the end of rotational acceleration (Fig. 2B). This latter observation in clap is in direct contrast to the peak in Le during fling, which was observed at the end of rotational acceleration. This disparity can be explained by examining the prescribed wing motion. In clap, wings were prescribed to translate first at a 45 deg angle of attack and then rotate. This provides ample time for the generation of shear layers around the bristles that block inter-bristle flow (see Kasoju et al., 2018 for a detailed discussion). Both rotation and translation started simultaneously in fling, necessitating more time for shear layers to develop around the bristles.

Maximum Le (Le_{max}) increased with increasing G and decreasing D (Fig. 7Bi,ii). However, changes in Le were comparatively small for the range of variation in G and D tested in this study. Similar to force coefficients (Fig. 4iii), increasing S did not show any particular trend for Le (Fig. 7Biii). However, if we look at the
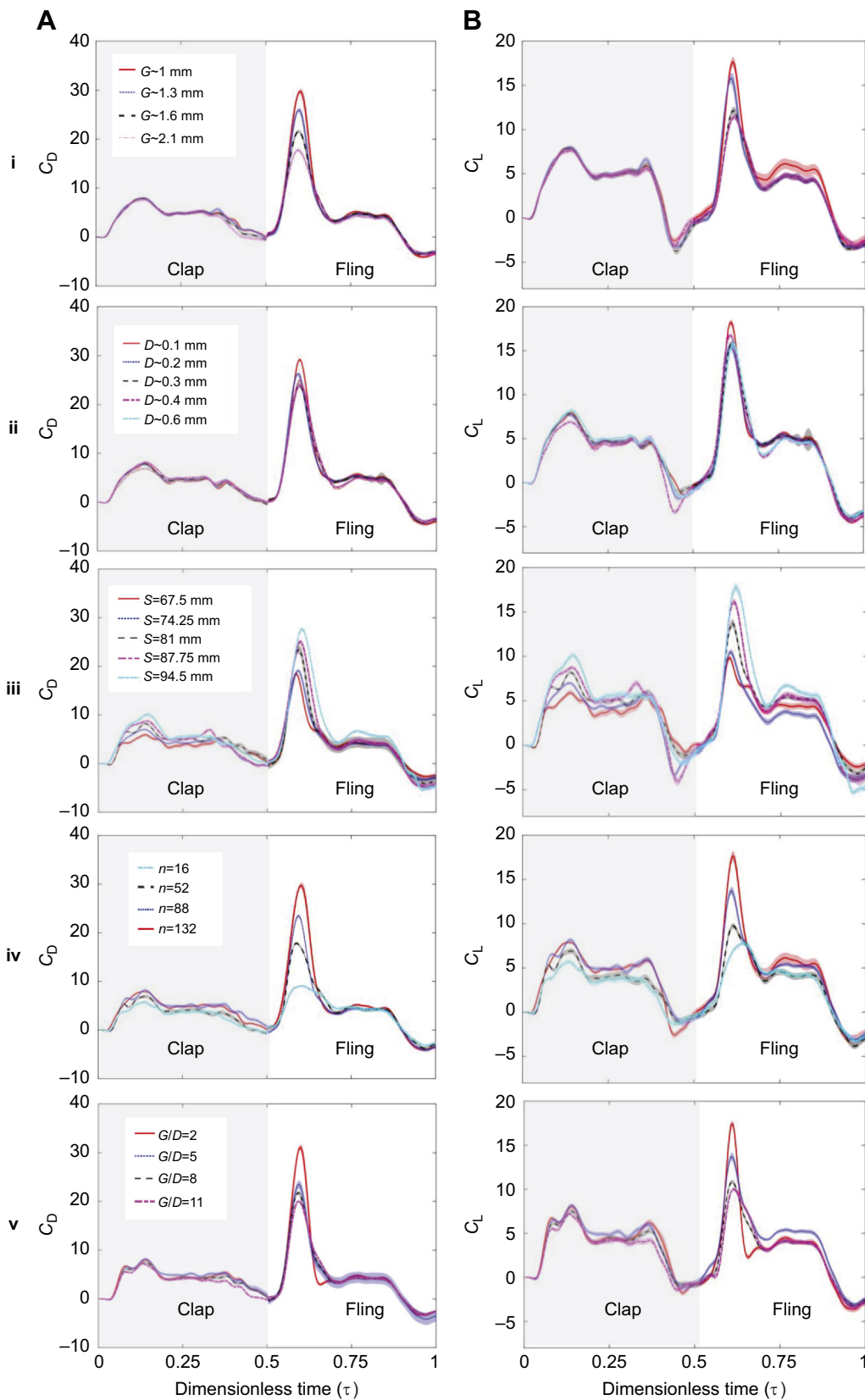
Fig. 4. Time-varying force coefficients during clap and fling at Re_c=10 with shading around each curve representing range of ±1 s.d. across 30 cycles. A and B show time-varying drag coefficient (C_D) and lift coefficient (C_L), respectively. From top to bottom, each row represents varying: (i) G, (ii) D, (iii) S, (iv) n and (v) G/D. Gray shaded region in each plot represents the clap phase, while unshaded region represents the fling phase. Re_c, Reynolds number based on wing chord.

extreme wingspans (67.5 and 94.5 mm), Le was found to increase with increasing S. Increasing n for constant G/D was found to decrease Le. Changing G/D for constant n showed little to no Le variation.

Chordwise flow characteristics

Velocity vector fields overlaid on out-of-plane vorticity contours (ω_z) showed the formation of LEV and TEV over the wing pair during clap and fling half-strokes (Movies 1–3). Vorticity in the
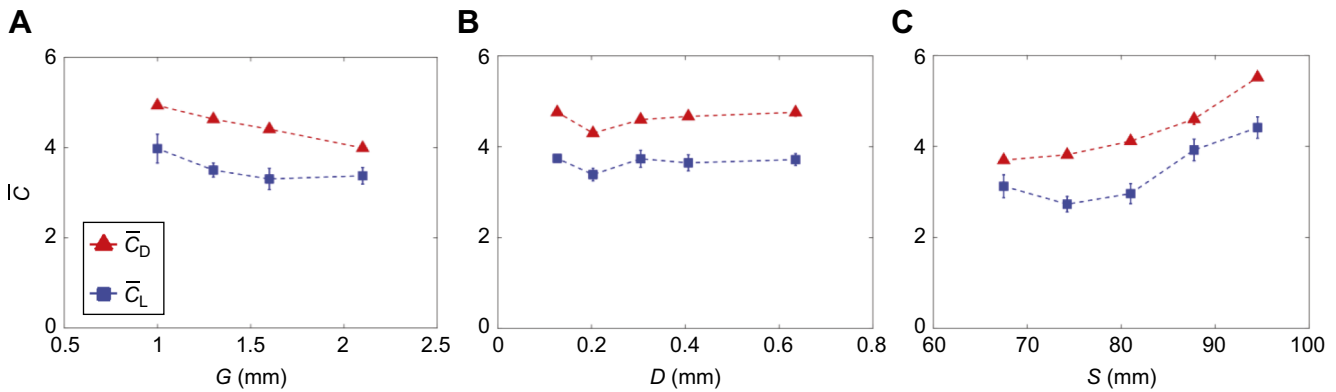
Fig. 5. Cycle-averaged force coefficients ($\bar{C}$) for varying G, D and S. Error bars corresponding to ±1 s.d. are included for every data point. A, B and C show average lift coefficient ($\bar{C}_L$) and average drag force coefficient ($\bar{C}_D$) for varying G, D and S, respectively. Estimates of s.d. for $\bar{C}_D$ and $\bar{C}_L$ for all conditions were <0.1 and <0.32, respectively.

LEV and TEV increased near the end of clap and in early fling, when the wings were in close proximity of each other (Fig. 8B–D). This suggests that wing–wing interaction plays an important role in LEV and TEV formation, which in turn impacts force generation. Circulation (Γ) of both the LEV and TEV showed little to no variation with changing G, D and S. Peak Γ for both the LEV and TEV occurred in fling (τ=0.65), near the end of both translational and rotational deceleration (Fig. 2B). This was followed by a decrease in Γ of both LEV and TEV with increasing fling time (Fig. 8B–D). Γ of the LEV and TEV increased slowly in time during clap and reached a maximum near the end of the clap (τ=0.35), corresponding to the start of translational deceleration and end of rotational acceleration. The latter was identical to the instant at which peak Γ occurred in fling.

From the prescribed kinematics (Fig. 2B), peak rotational acceleration started early in fling, whereas it started later in clap. This could be why Γ peaked early in fling and later in clap. This suggests that wing rotation plays a dominant role in LEV and TEV development. Also, both wings are in close proximity during the later stages of clap and early stages of fling, suggesting the importance of wing–wing interaction in LEV and TEV development. Thus, wing rotation in concert with wing–wing interaction augments LEV and TEV circulation during both clap and fling half-strokes.

DISCUSSION

Recent studies have shown that bristled wings provide drag reduction in clap-and-fling at Re_c relevant to tiny insect flight (Santhanakrishnan et al., 2014; Jones et al., 2016; Kasoju et al.,

2018; Ford et al., 2019). However, n, S_{max} and G/D had not been measured in different families of tiny insects, and their individual effects on aerodynamic forces were unclear. From our analysis of variation across thrips and fairyflies, we found that S_{max} and n increased with BL in both groups. We also found that G/D decreased with BL in both groups, but more strongly in thrips. Within the biologically relevant range of n and G/D, we found that: (1) increasing G provides more drag reduction as compared with decreasing D, (2) changing n for constant G/D has little variation on lift generation for n<100, and (3) changing G/D for constant n minimally impacts aerodynamic forces. The minimal influence of n and G/D on clap-and-fling aerodynamics, despite broad biological variation, suggests that tiny insects may experience lower biological pressure to functionally optimize n and G/D for a given wingspan.

Bristled wing morphology, evolutionary history and optimization

Variation among related species can stem from many factors: evolutionary history, correlated response in selection to other traits, physical constraints associated with body design and function, and adaptation to variation in body size, ecology or environment (Gould and Lewontin, 1979; Alexander, 1985; Taylor and Thomas, 2014). In the case of bristled wing morphology of tiny insects, most studies have examined physical constraints and adaptation, that is, whether interspecific variation has consequences for flight aerodynamics, possibly driven by variation in body size. For example, Ford et al. (2019) reported a narrow range of A_M/A_T (14–27%) across 25 thrips species, but much higher variation across fairyflies. In both groups, A_M/A_T showed a strong, positive relationship with body length.
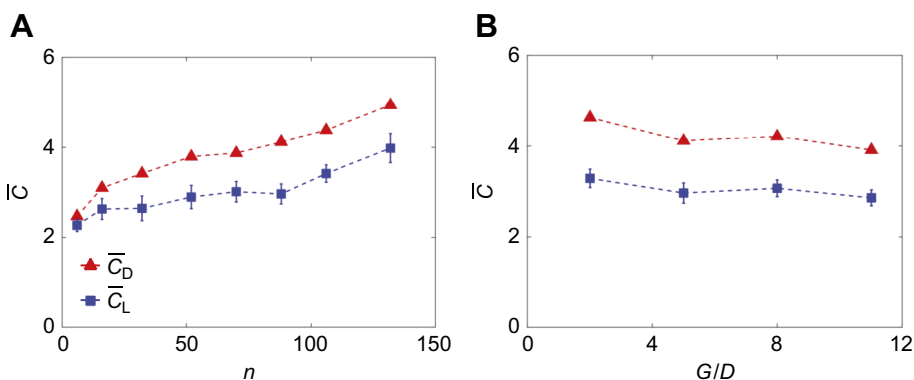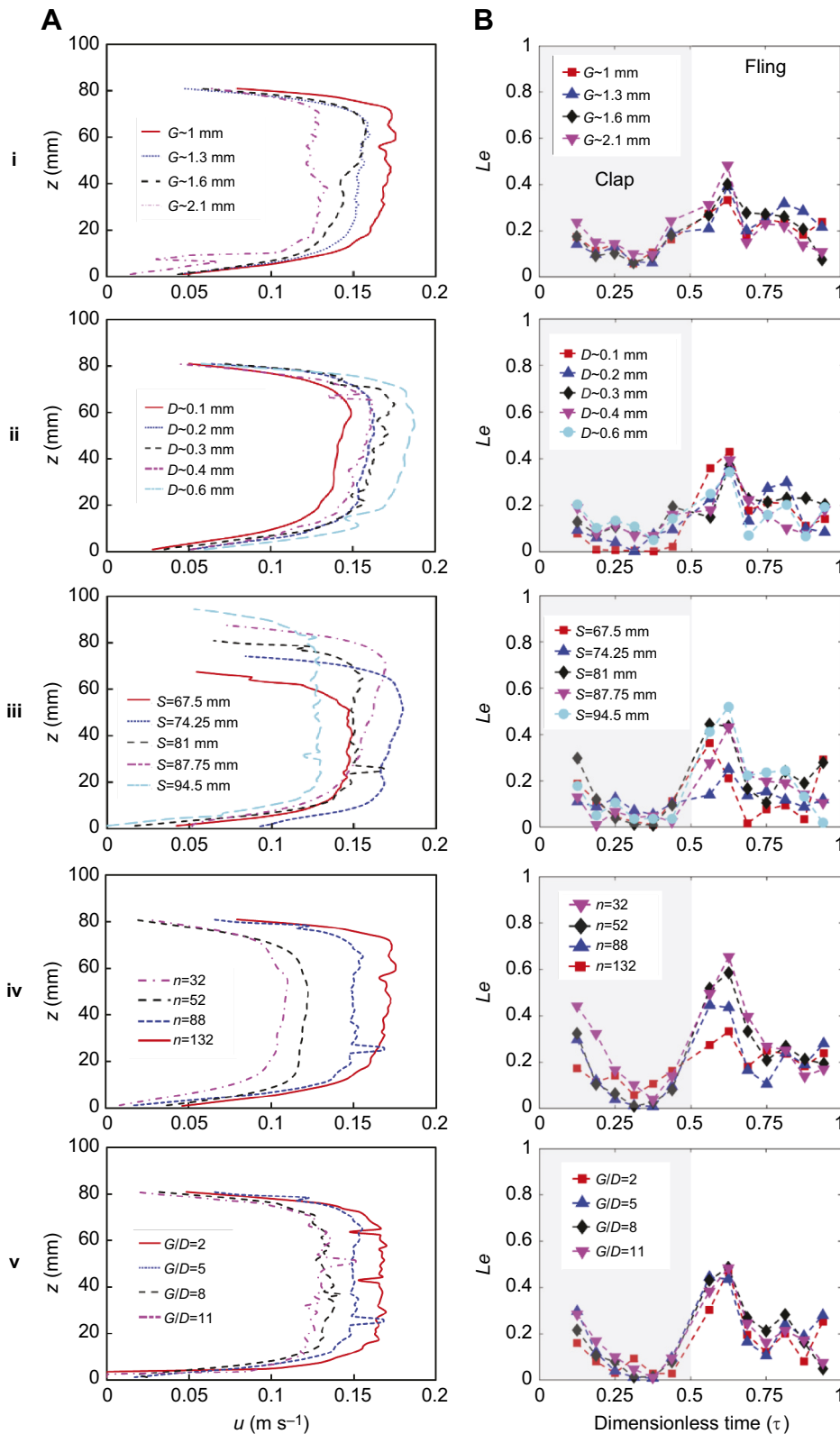

Fig. 6. Cycle-averaged force coefficients ($\bar{C}_L$, $\bar{C}_D$) as a function of n and G/D. (A) n and (B) G/D. Error bars corresponding to ±1 s.d. are included. Estimates of s.d. for $\bar{C}_D$ and $\bar{C}_L$ for all conditions were <0.1 and <0.32, respectively.

Fig. 7. Inter-bristle flow characteristics.
(A) Horizontal (i.e. *x*-component) velocity (*u*) variation along the wingspan (*z*-direction) during fling at $\tau \sim 0.63$. The velocity profile was extracted at a vertical line *l* oriented parallel to the wingspan, located at 5% chord length from the rightmost edge of the wing surface when viewing the wing along the *x*–*z* plane. (B) Time-variation of *Le*. From top to bottom, each row represents varying: (i) *G*, (ii) *D*, (iii) *S*, (iv) *n* and (v) *G/D*. The gray shaded region in B represents the clap phase and the unshaded region represents the fling phase.

At Re_{c} relevant to tiny insect flight, they found the highest aerodynamic efficiency (lift-to-drag ratio) for A_{M}/A_{T} in the range of thrips forewings and lower aerodynamic efficiency outside the range, perhaps facilitating flight in the larger-bodied thrips.

In this study, we found that both S_{max} and *n* increased with increasing BL in thrips and fairyflies (Fig. 1B,C). Interestingly, the ranges of S_{max} largely overlapped across fairyflies and thrips, despite differences in BL (most thrips BL>1 mm; all fairyfly BL<1 mm). This suggests that there could be a limit to the aerodynamic benefits of increasing wingspan. Moreover, we found that phylogenetic signal in the regression residuals (λ) was high for S_{max} on BL (Table 1), which explained the high R^2 value
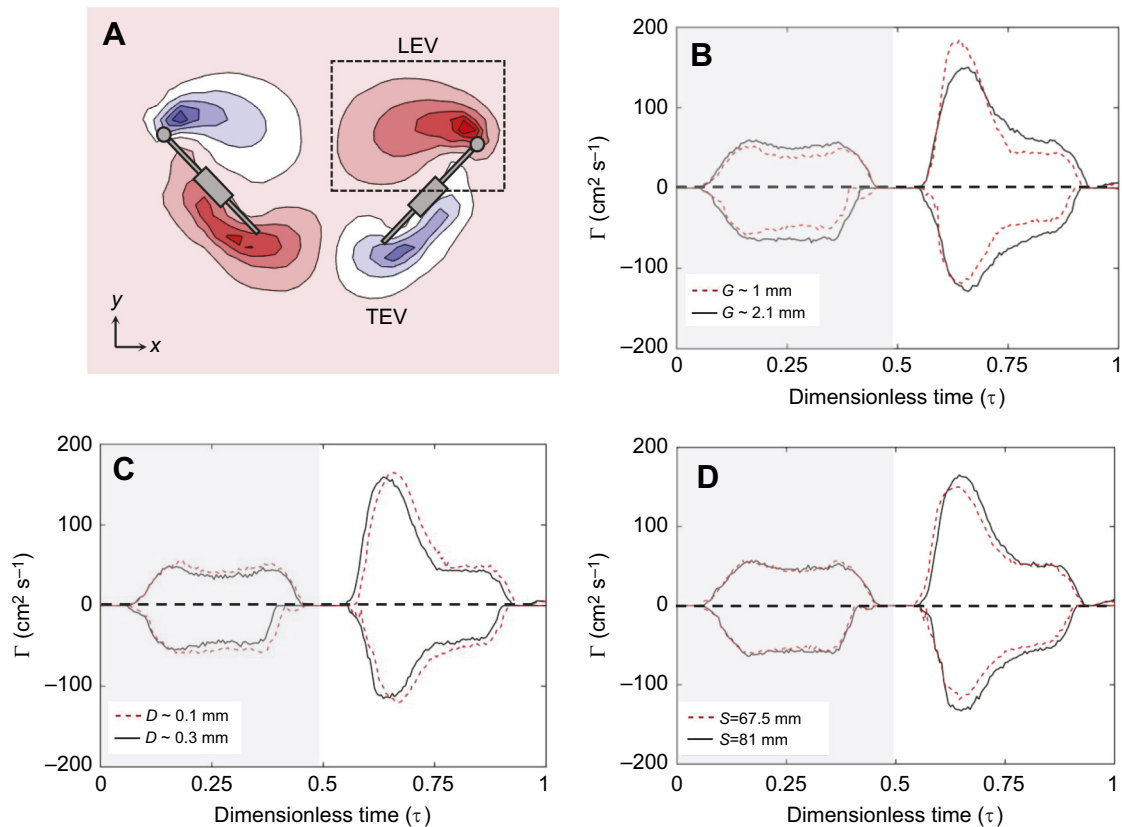
Fig. 8. Chordwise flow and circulation (Γ). (A) Representative out-of-plane component of vorticity (ω_z) during fling at $\tau=0.65$, obtained from processed TR-PIV data. Γ about the right wing was calculated by drawing a box around the LEV and TEV separately and integrating ω_z of the closed contour within each box. B, C and D show Γ during clap and fling for varying G, D and S, respectively. Positive circulation corresponds to TEV during clap and LEV during fling. Negative circulation corresponds to LEV during clap and TEV during fling.

despite much scatter about the regression line (i.e. phylogeny explained much of the residual variation in Fig. 1B). In other words, closely related species were similar in the way they deviated from the regression line (Revell, 2010), which suggests that underlying growth factors in common with BL may be ultimately driving variation in wingspan across closely related species. If selection favors a change in body size, then wingspan may similarly change.

Values of n were concentrated in the range of 60–90 for the species of thrips and fairyflies that we examined, corresponding to a large BL range of 300–1700 µm. Moreover, the relationship between n and BL was relatively weak ($R^2_{adj}=0.350$; Table 1). These observations led us to hypothesize that n may not need to be optimized to fall within a narrow range for a given BL toward improving aerodynamic performance. Consistent with this hypothesis, our robotic models showed insensitivity of aerodynamics to this range of n. The weak phylogenetic signal in regression residuals (Table 1) suggests little influence of evolutionary history (Hansen and Orzack, 2005). Therefore, the factors affecting the evolution of bristle number remain unclear.

Jones et al. (2016) previously showed no relationship between G/D and BL in fairyflies. However, our analyses suggest that there is an overall reduction in G/D with size in bristle-winged insects, with a steeper decline in thrips (Fig. 1D, Table 1). This difference in our results and those of Jones et al. (2016) stemmed from both our use of phylogenetic analyses and from including the larger thrips, which revealed an overall trend across taxa. That said, this pattern was still relatively weak ($R^2_{adj}=0.376$; Table 1), with much variation in G/D at a given BL. Previous studies have reported that both lift and drag forces

increase with decreasing G/D (Jones et al., 2016; Kasoju et al., 2018). This result could explain the more steeply negative relationship between G/D and BL in thrips, the larger of the two groups: as body mass increases, more lift is necessary to allow flight. Yet the high variation in G/D at long BL in fairyflies raises a question as to whether their G/D needs to be optimized for improving aerodynamic performance. In particular, we currently lack observations of fairyflies in free flight and thus do not know how or to what extent they use flapping flight. An intriguing possibility is that fairyflies facultatively parachute, and their wing structure better reflects the selective demands of that behavior. Thrips have been observed to facultatively parachute (Santhanakrishnan et al., 2014), increasing the probability that fairyflies do so as well.

Modeling considerations

Physical model studies of flapping flight match Re_c of the experiments to biological values to achieve dynamic similarity. Specific to the bristled wings of interest to this study, dynamic similarity of inter-bristle flow characteristics also necessitates matching Re_b to be in the range of tiny flying insects. When both Re_c and Re_b are matched between a physical bristled wing model to those of tiny insects, the scale model will produce non-dimensional forces similar to those of real insects. This is the major reason for presenting forces in term of non-dimensional coefficients throughout this study.

It has been reported that thrips (Kuethe, 1975) and the wasp *Encarsia formosa* (Ellington, 1975) operate at $Re_b=10^{-2}$ and 10^{-1}, respectively, and both at $Re_c\sim10$. With the exception of
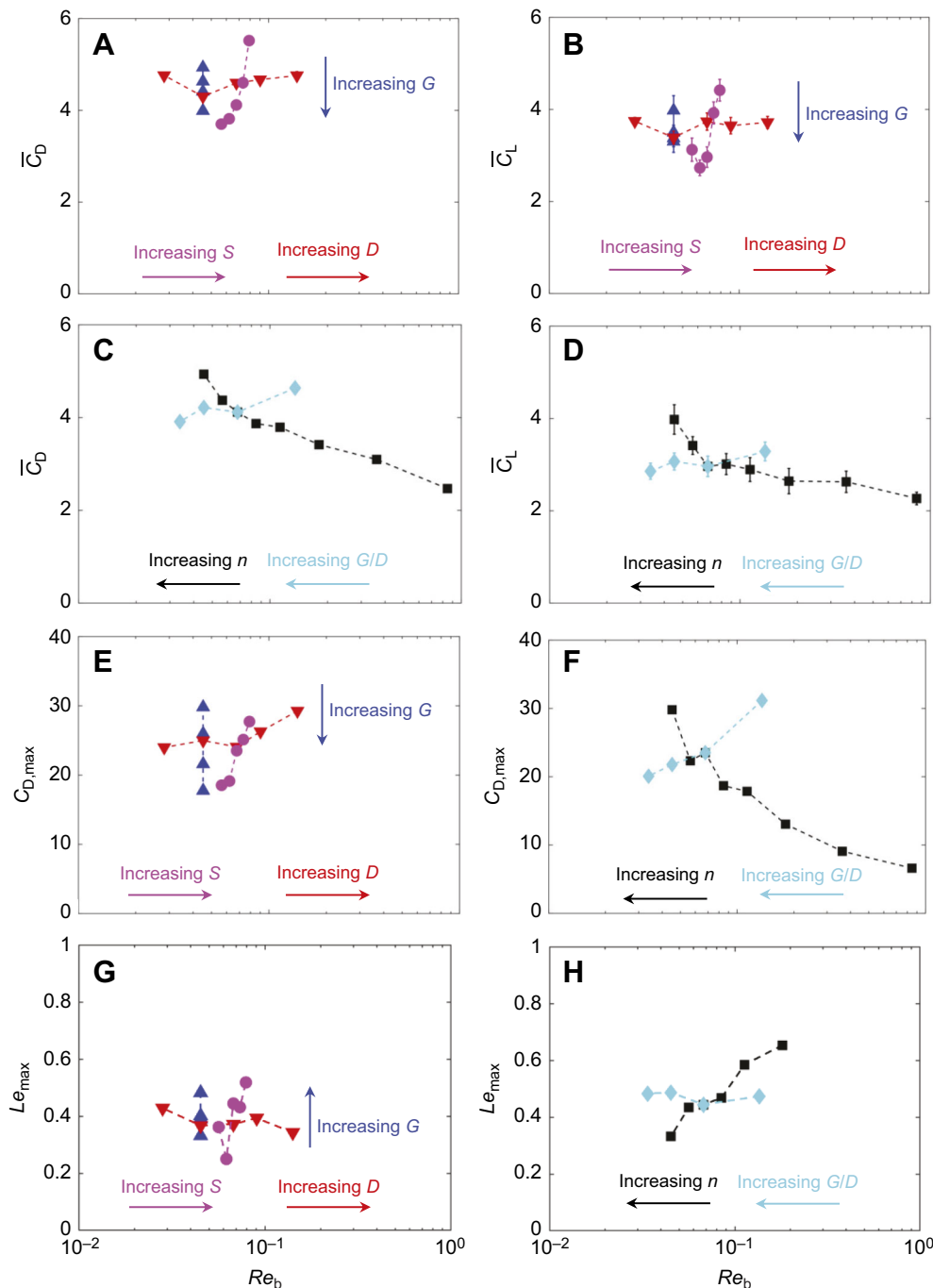
Fig. 9. Average force coefficients ($\bar{C}$), peak drag coefficient ($C_{D,max}$) and peak leakiness (Le_{max}) as a function of Reynolds number based on bristle diameter (Re_b). A and B show $\bar{C}_D$ and $\bar{C}_L$, respectively, for varying G, D and S. C and D show $\bar{C}_D$ and $\bar{C}_L$, respectively, for varying n and G/D. (E) $C_{D,max}$ for varying G, D and S. (F) $C_{D,max}$ for varying n and G/D. (G) Le_{max} for varying G, D and S. (H) Le_{max} for varying n and G/D. Re_b was calculated from the Reynolds number equation using bristle diameter (D) as the length scale. Trends with increasing geometric variables (G, D, S, n) and ratio (G/D) are indicated.

Jones et al. (2016), the majority of modeling studies of bristled wing aerodynamics (Sunada et al., 2002; Santhanakrishnan et al., 2014; Lee and Kim, 2017; Lee et al., 2018; Kasoju et al., 2018; Ford et al., 2019) only matched $Re_c \sim 10$ without matching Re_b to be relevant to tiny insects. Matching Re_b ensures that the flow through bristles of a model (and hence Le) would be similar to that of real insects. Considering that lift and drag are known to be impacted by the extent of leaky flow (Kasoju et al., 2018), we matched Re_b to fall within 0.01 to 0.1 in the majority of our physical models.

Varying G and D for fixed S

Previous studies proposed that the substantial drag reduction realized with bristled wings in clap-and-fling is due to fluid leaking through the bristles (Santhanakrishnan et al., 2014; Jones

et al., 2016; Kasoju et al., 2018). We found that Le peaked at $\tau \sim 0.56$ or $\tau \sim 0.63$ (Fig. 7B) for each condition of varying G and D, corresponding to the beginning of the fling phase. Interestingly, both $C_{D,max}$ and $C_{L,max}$ were observed between the same two time points, showing the importance of Le on dimensionless aerodynamic forces.

Previous studies of flow through bristled appendages found that Le is a function of both G and D (Cheer and Koehl, 1987; Hansen and Tiselius, 1992; Leonard, 1992; Loudon et al., 1994; Koehl, 1995). These studies also found that Le can change drastically for Re_b between 0.01 and 0.1, which is in the range of Re_b for tiny insects. We calculated Re_b for each wing model using D as the length scale in Eqn 2. Within the biological Re_b range (0.01–0.1), average force coefficients ($\bar{C}_D$, $\bar{C}_L$) showed no variation when

varying D (Fig. 9A,B). For experiments of varying G, we maintained D and S as constants. The calculated Re_b was identical for these tests and within the biological Re_b range. Therefore, for a constant Re_b, $\overline{C}_D$ can be varied significantly by varying G while maintaining minimal changes in $\overline{C}_L$ (Fig. 9A,B).

Increasing Re_b via varying D showed opposite trends in $C_{D,max}$ and Le_{max} (Fig. 9E,G). Within the biological Re_b range, increasing D decreased Le_{max} and increased $C_{D,max}$. Similarly, for a constant Re_b, increasing G increased Le_{max} and decreased $C_{D,max}$. These changes in leakiness for varying G and D are in agreement with previous studies (Cheer and Koehl, 1987; Loudon et al., 1994). Collectively, for Re_b in the range of tiny insects (0.01–0.1), we found that varying G provides drag reduction ($C_{D,max}$ and $\overline{C}_D$) as compared with varying D, by augmenting Le. Tiny insects could possibly meet their flight demands by modulating the inter-bristle gap. Ellington (1980) observed that dandelion thrips (*Thrips physapus*) open their forewing setae prior to take-off, suggesting that modulation of G may be possible when preparing for flight.

Little to no variation in $\overline{C}_L$ for both conditions (varying G and D) is attributed to formation of shear layers around the bristles that lowers the effective gap, resulting in the bristled wing behaving like a solid wing (Lee and Kim, 2017; Kasoju et al., 2018). Miller and Peskin (2005) proposed that LEV–TEV asymmetry plays a critical role in lift generation in clap-and-fling at $Re_c\sim10$. For varying G and varying D, we observed LEV circulation (Γ_{LEV}) to be larger compared with TEV circulation (Γ_{TEV}) for most of the clap-and-fling cycle (Fig. 8B,C). The implication of this asymmetry on lift generation can be seen by examining time-variation of C_L (Fig. 4Bi,ii), where positive C_L was observed for most of the cycle. Both Γ_{LEV} and Γ_{TEV} peaked at the same time point at which we observed peak C_L.

Varying *S* for fixed *n* and *G/D*
Several studies examining the aerodynamic effects of varying S have reported contradictory findings. Although some studies found little variation in force coefficients (Usherwood and Ellington, 2002; Luo and Sun, 2005; Garmann et al., 2013), others have postulated that longer wingspans are detrimental for force generation (Harbig et al., 2013; Han, Chang and Cho, 2015; Bhat et al., 2019). All these studies considered solid wings at $Re_c>100$. Our study is the first to report the effect of varying S on the aerodynamic performance of bristled wings performing clap-and-fling at $Re_c=10$. Within the biological Re_b range, both $\overline{C}_D$ and $\overline{C}_L$ were found to increase with S (Fig. 9A,B). In addition, $C_{D,max}$ and Le_{max} increased with increasing S (Fig. 9E,G).

The increase in G when increasing S is expected to increase Le and lower drag. However, we found that increasing S increased both Le and drag. Increasing S increases the wing surface area, which can explain the increase in drag. In addition, increasing G also increases Le. We speculate that the increase in Le with increasing S would minimize the increase in drag that would be expected from increasing wing surface area. Separately, varying S showed little change in Γ_{LEV} and Γ_{TEV} (Fig. 8D), which resulted in small changes in C_L (Fig. 4Biii). Within the biological range of n, G/D and Re_b, we postulate that larger S might be particularly beneficial to tiny insects when parachuting (Santhanakrishnan et al., 2014), as larger drag can slow their descent.

Varying *n* for fixed *G/D* and *S*
$\overline{C}_D$ substantially increased with increasing n, while $\overline{C}_L$ showed minimal variation for $n\leq88$ and then increased with further increases in n (Fig. 6A). Wing models with $n\leq88$ showed better

aerodynamic performance in terms of force generation as compared with models with $n>88$. Interestingly, forewing morphological analysis showed that values of n were concentrated in the region of 30–90 for thrips and fairyflies. Moreover, $\overline{C}_D$ generated for this dominant range of n was larger than $\overline{C}_D$ generated for $n=6$ and 16. Thrips have been observed to intermittently parachute (Santhanakrishnan et al., 2014), likely to lower the energetic demands of flapping flight and potentially also during wind-assisted long-distance dispersal (Horridge, 1956). During parachuting, these larger drag forces can assist them in migrating longer distances (Morse and Hoddle, 2006). In addition, our morphological measurements showed that n varied from 32 to 161 across species, so lower n may better assist in generating lift needed for active flight, whereas larger n may better generate drag needed for passive dispersal via parachuting. Currently, it is unknown whether species with larger n tend to parachute more often.

Large variation in $C_{D,max}$ and Le_{max} with n (Fig. 9F,H) showed the influence of the number of bristles on aerodynamic performance. Le_{max} decreased with increasing n, while $C_{D,max}$ increased with increasing n. This suggests that changing n can aid or hinder aerodynamic performance by altering the leaky flow through the bristles. However, within the biological range of Re_b and n, only marginal changes in $\overline{C}_L$ in comparison with $\overline{C}_D$ were observed (Fig. 9C,D). This suggests that for a fixed S and G/D, tiny insects may experience reduced biological pressure to fit a particular number of bristles for adequate lift generation. This inference is also supported by the broad interspecific variation in n (Fig. 1C).

Varying *G/D* for fixed *n* and S
Within the biological Re_b range, $C_{D,max}$ and Le_{max} were found to minimally change with increasing G/D (Fig. 9F,H). Also, varying G/D within the biological Re_b range produced little to no variation in $\overline{C}_D$ and $\overline{C}_L$. Note that for varying G/D within the biological Re_b range, the inter-bristle gap in the corresponding physical models was nearly identical, which likely explains the minimal change in Le_{max}. From these results, we summarize that within the biological range of Re_b, G/D variation for a fixed S, n and G results in little variation in aerodynamic force generation.

Morphological measurements showed that G/D in thrips decreased with increasing BL, while the relationship was shallower for fairyflies. This dissimilar result in fairyflies and thrips raises a question regarding our use of static wing images for G/D measurements as opposed to free-flight wing images. We were restricted to using static forewing images owing to the lack of free-flight wing images of tiny insects with adequate (i.e. high) magnification. It is unknown at present whether tiny insects can modulate G/D during free flight, as such a capability could permit them to tailor aerodynamic forces in relation to ambient conditions (e.g. temperature, humidity, wind speed) and associated energetic costs.

Future directions
We see many directions for future work. First, many bristle-winged insects show asymmetry in wing shape (Fig. 1; Jones et al., 2016). We did not consider the effects of the asymmetry in L_b on either side of the forewing (i.e. leading edge and trailing edge) or of bristle angle relative to the horizontal. Asymmetry in L_b within the biological Re_b range may not noticeably affect clap-and-fling aerodynamics, because damage may occur to the wing bristles during an insect's life and biological systems are often robust to such perturbations. Nonetheless, this may be a worthwhile direction for future work. Similarly, our physical models did not account for variation in wing shape and were simplified to a rectangular planform. There is much

additional diversity in wing shape, especially when comparing fairyflies (teardrop-shaped) with thrips (smaller chord relative to span; Ford et al., 2019). At Re_c=10, changes in wing shape did not significantly affect the trend of aerodynamic force generation in time during clap-and-fling (comparing lift and drag force generation of rectangular bristled wing pairs used in Kasoju et al., 2018 to approximately elliptical bristled wing pairs used in Ford et al., 2019). However, the possible effects of wing shape on flying in bristle-winged insects – particularly across body sizes – would be valuable to study. Finally, the bristles on the wings of these insects are considerably flexible, yet we suspect them to behave stiffer in motion owing to high viscous forces. This was also evident with the stainless-steel wires that we used as bristles. Although these wires looked very flexible in air, the wires did not flex when tested in glycerin. We chose bristles that did not flex during motion because no quantitative data are available on flexibility of bristles in tiny insects. Based on published high-speed video of thrips (Santhanakrishnan et al., 2014; Cheng and Sun, 2018; Lyu et al., 2019), it is evident they flex their wings along the spanwise direction when flinging their wings apart at the start of downstroke. Because the variability in the wing flexibility along the wingspan has not yet been characterized in any published study, we used rigid wing models. Future studies are needed to document interspecific diversity in wing shape and flexibility to examine how they might affect aerodynamic forces.

Conclusions
Our analysis of forewing morphology in thrips and fairyflies showed similar scaling relationships between the two groups in the variables tested (n, G/D and S_{max}). Within the biologically relevant range of Re_b (0.01–0.1) for tiny insects, we observed that increasing the inter-bristle spacing (G) for fixed bristle diameter (D) decreased drag forces significantly. This was supported by a significant increase in leakiness observed during early fling. However, changes in average lift forces were minimal, suggesting that having the capability of increasing the inter-bristle spacing during free flight could help these insects to overcome large drag forces with minimal changes in lift force. We also found that varying bristle diameter (D) had no effect on aerodynamic force generation, and varying the non-dimensional inter-bristle gap-to-diameter ratio (G/D) showed no significant influence on aerodynamic force generation. Finally, although we found that drag forces significantly decreased with decreasing number of bristles (n), lift force only minimally changed for $n<100$. At $n>100$, we observed a significant jump in lift forces. Considering the broad variation of n (32–161) observed across species, the lack of change in lift forces for $n<100$ suggests that tiny insects may experience less biological pressure to optimize n for a given wingspan. Alternatively, stabilizing selection may maintain species within a range of values that does not affect flight performance.

Data availability
All supplementary R code and data are available in the Figshare Digital Repository: https://doi.org/10.6084/m9.figshare.14478108.v1.

References
Alexander, R. M. (1985). The ideal and the feasible: physical constraints on evolution. *Biol. J. Linn. Soc.* **26**, 345-358. doi:10.1111/j.1095-8312.1985.tb02046.x

Arora, N., Gupta, A., Sanghi, S., Aono, H. and Shyy, W. (2014). Lift-drag and flow structures associated with the "clap and fling" motion. *Phys. Fluids* **26**, 071906. doi:10.1063/1.4890221

Bhat, S. S., Zhao, J., Sheridan, J., Hourigan, K. and Thompson, M. C. (2019). Uncoupling the effects of aspect ratio, Reynolds number and Rossby number on a rotating insect-wing planform. *J. Fluid Mech.* **859**, 921-948. doi:10.1017/jfm.2018.833

Birch, J. M., Dickson, W. B. and Dickinson, M. H. (2004). Force production and flow structure of the leading edge vortex on flapping wings at high and low Reynolds numbers. *J. Exp. Biol.* **207**, 1063-1072. doi:10.1242/jeb.00848

Blount, Z. D., Lenski, R. E. and Losos, J. B. (2018). Contingency and determinism in evolution: replaying life's tape. *Science* **362**, eaam5979. doi:10.1126/science.aam5979

Buckman, R. S., Mound, L. A. and Whiting, M. F. (2013). Phylogeny of thrips (Insecta: Thysanoptera) based on five molecular loci. *Syst. Entomol.* **38**, 123-133. doi:10.1111/j.1365-3113.2012.00650.x

Burnham, K. P. and Anderson, D. R. (2002). *Model Selection and Multimodel Inference: A Practical Information-Theoretic Approach.* New York: Springer-Verlag.

Cavalleri, A. and Mound, L. A. (2012). Toward the identification of *Frankliniella* species in Brazil (Thysanoptera, Thripidae). *Zootaxa* **3270**, 1-30. doi:10.11646/zootaxa.3270.1.1

Cavalleri, A. and Mound, L. A. (2014). The neotropical flower-living genus *Lenkothrips* (Thysanoptera, Heterothripidae): three new species and an identification key. *Zootaxa* **3814**, 581-590. doi:10.11646/zootaxa.3814.4.9

Cavalleri, A., Lindner, M. F. and Mendonça, M. D. S., Jr (2016). New Neotropical Haplothripini (Thysanoptera: Phlaeothripidae) with a key to Central and South American genera. *J. Nat. Hist.* **50**, 1389-1410. doi:10.1080/00222933.2015.1113316

Cheer, A. Y. L. and Koehl, M. A. R. (1987). Paddles and rakes: fluid flow through bristled appendages of small organisms. *J. Theor. Biol.* **129**, 17-39. doi:10.1016/S0022-5193(87)80201-1

Cheng, X. and Sun, M. (2018). Very small insects use novel wing flapping and drag principle to generate the weight-supporting vertical force. *J. Fluid Mech.* **855**, 646-670. doi:10.1017/jfm.2018.668

Dang, L.-H., Mound, L. A. and Qiao, G.-X. (2014). Conspectus of the Phlaeothripinae genera from China and Southeast Asia (Thysanoptera, Phlaeothripidae). *Zootaxa* **3807**, 1-82. doi:10.11646/zootaxa.3807.1.1

Davis, R. B., Baldauf, S. L. and Mayhew, P. J. (2010). The origins of species richness in the Hymenoptera: insights from a family-level supertree. *BMC Evol. Biol.* **10**, 109. doi:10.1186/1471-2148-10-109

Dickinson, M. H., Lehmann, F. O. and Sane, S. P. (1999). Wing rotation and the aerodynamic basis of insect flight. *Science* **284**, 1954-1960. doi:10.1126/science.284.5422.1954

Ellington, C. P. (1975). *Swimming and Flying in Nature*, Vol. 2. New York: Plenum Press.

Ellington, C. P. (1980). Wing mechanics and take-off preparation of thrips (Thysanoptera). *J. Exp. Biol.* **85**, 129-136. doi:10.1242/jeb.85.1.129

Ford, M. P., Kasoju, V. T., Gaddam, M. G. and Santhanakrishnan, A. (2019). Aerodynamic effects of varying solid surface area of bristled wings performing clap and fling. *Bioinspir. Biomim.* **14**, 046003. doi:10.1088/1748-3190/ab1a00

Freckleton, R. P., Harvey, P. H. and Pagel, M. (2002). Phylogenetic analysis and comparative data: a test and review of evidence. *Am. Nat.* **160**, 712-726. doi:10.1086/343873

Futuyma, D. J. and Kirkpatrick, M. (2017). *Evolution*. Sunderland, MA: Sinauer Associates.

Garmann, D. J., Visbal, M. R. and Orkwis, P. D. (2013). Three-dimensional flow structure and aerodynamic loading on a revolving wing, *Phys. Fluids* **25**, 034101. doi:10.1063/1.4794753

Gartner, G. E. A., Hicks, J. W., Manzani, P. R., Andrade, D. V., Abe, A. S., Wang, T., Secor, S. M. and Garland, T., Jr (2010). Phylogeny, ecology, and heart position in snakes. *Physiol. Biochem. Zool.* **83**, 43-54. doi:10.1086/648509

Gibson, G. A. P., Read, J. and Huber, J. T. (2007). Diversity, classification and higher relationships of Mymarommatoidea (Hymenoptera). *J. Hymenoptera Res.* **16**, 51-146.

Glazier, D. S. (2021). Biological scaling analyses are more than statistical line fitting. *J. Exp. Biol.* **224**, jeb241059. doi:10.1242/jeb.241059

Goldaracena, A. and Hance, T. (2017). A new species of *Frankliniella* with 7-segmented antennae from Mexico (Thysanoptera, Thripinae). *Zootaxa* **4231**, 145-150. doi:10.11646/zootaxa.4231.1.12

Gould, S. J. (2002). *The Structure of Evolutionary Theory.* Cambridge, MA: Belknap Press, Harvard University Press.

Gould, S. J. and Lewontin, R. C. (1979). The spandrels of San Marco and the Panglossian paradigm: a critique of the adaptationist programme. *Proc. R. Soc. B* **205**, 581-598. doi:10.1098/rspb.1979.0086

Han, J.-S., Chang, J. W. and Cho, H.-K. (2015). Vortices behavior depending on the aspect ratio of an insect-like flapping wing in hover. *Exp. Fluids* **56**, 181. doi:10.1007/s00348-015-2049-9

Hansen, T. F. and Orzack, S. H. (2005). Assessing current adaptation and phylogenetic inertia as explanations of trait evolution: the need for controlled comparisons. *Evolution* **59**, 2063-2072. doi:10.1554/05-088.1

Hansen, B. and Tiselius, P. (1992). Flow through the feeding structures of suspension feeding zooplankton: a physical model approach. *J. Plankton Res.* **14**, 821-834. doi:10.1093/plankt/14.6.821

Harbig, R. R., Sheridan, J. and Thompson, M. C. (2013). Reynolds number and aspect ratio effects on the leading-edge vortex for rotating insect wing planforms. *J. Fluid Mech.* **717**, 166-192. doi:10.1017/jfm.2012.565

Heraty, J. M., Burks, R. A., Cruaud, A., Gibson, G. A. P., Liljeblad, J., Munro, J., Rasplus, J.-Y., Delvare, G., Janšta, P., Gumovsky, A. et al. (2013). A phylogenetic analysis of the megadiverse Chalcidoidea (Hymenoptera). *Cladistics* **29**, 466-542. doi:10.1111/cla.12006

Ho, L. T., Ané, C. (2014). A linear-time algorithm for Gaussian and non-Gaussian trait evolution models. *Syst. Biol.* **63**, 397-408. doi:10.1093/sysbio/syu005

Horridge, G. A. (1956). The flight of very small insects. *Nature* **178**, 1334-1335. doi:10.1038/1781334a0

Housworth, E. A. and Martins, E. P. (2001). Random sampling of constrained phylogenies: conducting phylogenetic analyses when the phylogeny is partially known. *Syst. Biol.* **50**, 628-639. doi:10.1080/106351501753328776

Huber, J. T. (1986). Systematics, biology, and hosts of the Mymaridae and Mymarommatidae (Insecta: Hymenoptera). *Entomography* **4**, 185-243.

Huber, J. T. (2005). The gender and derivation of genus-group names in Mymaridae and Mymarommatidae (Hymenoptera). *Acta Soc. Zool. Bohem.* **69**, 167-183.

Huber, J. T. (2017). *Eustochomorpha* Girault, *Neotriadomerus* gen. n., and *Proarescon* gen. n. (Hymenoptera, Mymaridae), early extant lineages in evolution of the family. *J. Hymenopt. Res.* **57**, 1-87. doi:10.3897/jhr.57.12892

Huber, J. T. and Baquero, E. (2007). Review of *Eustochus*, a rarely collected genus of Mymaridae (Hymenoptera). *J. Entomol. Soc. Ont.* **138**, 3-31.

Huber, J. T. and Noyes, J. S. (2013). A new genus and species of fairyfly, *Tinkerbella nana* (Hymenoptera, Mymaridae), with comments on its sister genus *Kikiki*, and discussion on small size limits in arthropods. *J. Hymenopt. Res.* **32**, 17-44. doi:10.3897/jhr.32.4663

Huber, J. T., Mendel, Z., Protasov, A. and La Salle, J. (2006). Two new Australian species of *Stethynium* (Hymenoptera: Mymaridae), larval parasitoids of *Ophelimus maskelli* (Ashmead) (Hymenoptera: Eulophidae) on eucalyptus. *J. Nat. Hist.* **40**, 1909-1921. doi:10.1080/00222930601046428

Huber, J. T., Gibson, G. A. P., Bauer, L. S., Liu, H. and Gates, M. (2008). The genus *Mymaromella* (Hymenoptera: Mymarommatidae) in North America, with a key to described extant species. *J. Hymenopt. Res.* **17**, 175-194.

Jones, D. R. (2005). Plant viruses transmitted by thrips. *Eur. J. Plant Pathol.* **113**, 119-157. doi:10.1007/s10658-005-2334-1

Jones, S. K., Yun, Y. J. J., Hedrick, T. L., Griffith, B. E. and Miller, L. A. (2016). Bristles reduce the force required to 'fling' wings apart in the smallest insects. *J. Exp. Biol.* **219**, 3759-3772. doi:10.1242/jeb.143362

Kasoju, V. T. and Santhanakrishnan, A. (2021). Aerodynamic interaction of bristled wing pairs in fling. *Phys. Fluids* **33**, 031901. doi:10.1063/5.0036018

Kasoju, V. T., Terrill, C. L., Ford, M. P. and Santhanakrishnan, A. (2018). Leaky flow through simplified physical models of bristled wings of tiny insects during clap and fling. *Fluids* **3**, 44. doi:10.3390/fluids3020044

Koehl, M. A. (1995). Fluid flow through hair-bearing appendages: feeding, smelling and swimming at low and intermediate Reynolds numbers. *Symp. Soc. Exp. Biol.* **49**, 157-182.

Kuethe, A. M. (1975). *Swimming and Flying in Nature*, Vol. 2. New York: Plenum Press.

Lee, S. H. and Kim, D. (2017). Aerodynamics of a translating comb-like plate inspired by a fairyfly wing. *Phys. Fluids* **29**, 081902. doi:10.1063/1.4998434

Lee, S. H., Lahooti, M. and Kim, D. (2018). Aerodynamic characteristics of unsteady gap flow in a bristled wing. *Phys. Fluids* **30**, 071901. doi:10.1063/1.5030693

Lehmann, F.-O. and Pick, S. (2007). The aerodynamic benefit of wing-wing interaction depends on stroke trajectory in flapping insect wings. *J. Exp. Biol.* **210**, 1362-1377. doi:10.1242/jeb.02746

Lehmann, F.-O., Sane, S. P. and Dickinson, M. (2005). The aerodynamic effects of wing-wing interaction in flapping insect wings. *J. Exp. Biol.* **208**, 3075-3092. doi:10.1242/jeb.01744

Leonard, A. B. P. (1992). The biomechanics, autecology and behavior of suspension-feeding in crinoid echinoderms. *PhD dissertation*. University of California, San Diego.

Lighthill, M. J. (1973). On the Weis-Fogh mechanism of lift generation. *J. Fluid Mech.* **60**, 1-17. doi:10.1017/S0022112073000017

Lima, É. F. B. and Mound, L. A. (2016a). Species-richness in Neotropical Sericothripinae (Thysanoptera: Thripidae). *Zootaxa* **4162**, 1-45. doi:10.11646/zootaxa.4162.1.1

Lima, É. F. B. and Mound, L. A. (2016b). Systematic relationships of the Thripidae subfamily Sericothripinae (Insecta: Thysanoptera). *Zool. Anz.* **263**, 24-32. doi:10.1016/j.jcz.2016.03.001

Lin, N. Q., Huber, J. T. and LaSalle, J. (2007). The Australian genera of Mymaridae (Hymenoptera: Chalcidoidea). *Zootaxa* **1596**, 1-111. doi:10.11646/zootaxa.1596.1.1

Losos, J. B. (1994). An approach to the analysis of comparative data when a phylogeny is unavailable or incomplete. *Syst. Biol.* **43**, 117-123. doi:10.1093/sysbio/43.1.117

Loudon, C., Best, B. A. and Koehl, M. A. R. (1994). When does motion relative to neighboring surfaces alter the flow through arrays of hairs? *J. Exp. Biol.* **193**, 233-254. doi:10.1242/jeb.193.1.233

Luo, G. and Sun, M. (2005). The effects of corrugation and wing planform on the aerodynamic force production of sweeping model insect wings. *Acta Mech. Sinica* **21**, 531-541. doi:10.1007/s10409-005-0072-4

Lyu, Y. Z., Zhu, H. J. and Sun, M. (2019). Flapping-mode changes and aerodynamic mechanisms in miniature insects. *Physical Rev. E* **99**, 012419. doi:10.1103/PhysRevE.99.012419

Martins, E. P. (1996). Conducting phylogenetic comparative studies when the phylogeny is not known. *Evolution* **50**, 12-22. doi:10.1111/j.1558-5646.1996.tb04468.x

Martins, E. P. and Hansen, T. F. (1997). Phylogenies and the comparative method: a general approach to incorporating phylogenetic information into the analysis of interspecific data. *Am. Nat.* **149**, 646-667. doi:10.1086/286013

Martins, E. P. and Housworth, E. A. (2002). Phylogeny shape and the phylogenetic comparative method. *Syst. Biol.* **51**, 873-880. doi:10.1080/10635150290102573

Masumoto, M., Ng, Y. F. and Okajima, S. (2013). A new genus of Thripinae (Thysanoptera, Thripidae) collected from *Pandanus* in Japan, Malaysia and Australia, with three new species. *Zootaxa* **3709**, 543-554. doi:10.11646/zootaxa.3709.6.3

Miller, L. A. and Peskin, C. S. (2004). When vortices stick: an aerodynamic transition in tiny insect flight. *J. Exp. Biol.* **207**, 3073-3088. doi:10.1242/jeb.01138

Miller, L. A. and Peskin, C. S. (2005). A computational fluid dynamics study of 'clap and fling' in the smallest insects. *J. Exp. Biol.* **208**, 195-212. doi:10.1242/jeb.01376

Miller, L. A. and Peskin, C. S. (2009). Flexible clap and fling in tiny insect flight. *J. Exp. Biol.* **212**, 3076-3090. doi:10.1242/jeb.028662

Minaei, K. and Aleosfoor, M. (2013). A new species of *Haplothrips* from southern Iran (Thysanoptera, Phlaeothripidae). *Zookeys* **275**, 91-99. doi:10.3897/zookeys.275.4433

Moen, D. S., Irschick, D. J. and Wiens, J. J. (2013). Evolutionary conservatism and convergence both lead to striking similarity in ecology, morphology, and performance across continents in frogs. *Proc. R. Soc. Long. B* **280**, 20132156. doi:10.1098/rspb.2013.2156

Moen, D. S., Morlon, H. and Wiens, J. J. (2016). Testing convergence versus history: convergence dominates phenotypic evolution for over 150 million years in frogs. *Syst. Biol.* **65**, 146-160. doi:10.1093/sysbio/syv073

Morse, J. G. and Hoddle, M. S. (2006). Invasion biology of thrips. *Annu. Rev. Entomol.* **51**, 67-89. doi:10.1146/annurev.ento.51.110104.151044

Mound, L. A. (2009). New taxa and new records of Australian Panchaetothripinae (Thysanoptera, Thripidae). *Zootaxa* **2292**, 25-33. doi:10.11646/zootaxa.2292.1.3

Mound, L. A. and Reynaud, P. (2005). *Franklinothrips*; a pantropical Thysanoptera genus of ant-mimicking obligate predators (Aeolothripidae). *Zootaxa* **864**, 1-16. doi:10.11646/zootaxa.864.1.1

Mound, L. A. and Tree, D. J. (2016). Genera of the leaf-feeding Dendrothripinae of the world (Thysanoptera, Thripidae), with new species from Australia and Sulawesi, Indonesia. *Zootaxa* **4109**, 569-582. doi:10.11646/zootaxa.4109.5.5

Munro, J. B., Heraty, J. M., Burks, R. A., Hawks, D., Mottern, J., Cruaud, A., Rasplus, J.-Y. and Jansta, P. (2011). A molecular phylogeny of the Chalcidoidea (Hymenoptera). *PLoS ONE* **6**, e27023. doi:10.1371/journal.pone.0027023

Ng, Y. F. and Mound, L. A. (2015). Species of Thripinae (Thysanoptera) from bamboo in Malaysia, with one new species and six new records. *Zootaxa* **3918**, 492-502. doi:10.11646/zootaxa.3918.4.2

Pagel, M. (1999). Inferring the historical patterns of biological evolution. *Nature* **401**, 877-884. doi:10.1038/44766

Pélabon, C., Firmat, C., Bolstad, G. H., Voje, K. L., Houle, D., Cassara, J., Rouzic, A. L. and Hansen, T. F. (2014). Evolution of morphological allometry. *Ann. N Y Acad. Sci.* **1320**, 58-75. doi:10.1111/nyas.12470

Pereyra, V., Cavalleri, A., Szumik, C. and Weirauch, C. (2019). Phylogenetic analysis of the New World family Heterothripidae (Thysanoptera, Terebrantia)

based on morphological and molecular evidence. *Insect Syst. Evol.* **50**, 702-716. doi:10.1163/1876312X-00002193

Poinar, G., , Jr and Huber, J. T. (2011). A new genus of fossil Mymaridae (Hymenoptera) from Cretaceous amber and key to Cretaceous mymarid genera. *Zookeys* **130**, 461-472. doi:10.3897/zookeys.130.1241

Polilov, A. A. (2015). Small is beautiful: features of the smallest insects and limits to miniaturization. *Annu. Rev. Entomol.* **60**, 103-121. doi:10.1146/annurev-ento-010814-020924

Posada, D. and Buckley, T. R. (2004). Model selection and model averaging in phylogenetics: advantages of Akaike information criterion and Bayesian approaches over likelihood ratio tests. *Syst. Biol.* **53**, 793-808. doi:10.1080/10635150490522304

Revell, L. J. (2010). Phylogenetic signal and linear regression on species data. *Methods Ecol. Evol.* **1**, 319-329. doi:10.1111/j.2041-210X.2010.00044.x

Revell, L. J. (2012). phytools: an R package for phylogenetic comparative biology (and other things). *Methods Ecol. Evol.* **3**, 217-223. doi:10.1111/j.2041-210X.2011.00169.x

Riley, D. G., Joseph, S. V., Srinivasan, R. and Diffie, S. (2011). Thrips vectors of tospoviruses. *J. Integr. Pest Manag.* **2**, I1-I10. doi:10.1603/IPM10020

Rodriguez-Saona, C. R., Polavarapu, S., Barry, J. D., Polk, D., Jörnsten, R., Oudemans, P. V. and Liburd, O. E. (2010). Color preference, seasonality, spatial distribution and species composition of thrips (Thysanoptera: Thripidae) in northern highbush blueberries. *Crop Prot.* **29**, 1331-1340. doi:10.1016/j.cropro.2010.07.006

Rohlf, F. J. (2006). A comment onphylogenetic correction. *Evolution* **60**, 1509-1515. doi:10.1554/05-550.1

Samaee, M., Nelsen, N. H., Gaddam, M. G. and Santhanakrishnan, A. (2020). Diastolic vortex alterations with reducing left ventricular volume: an *in vitro* study. *J. Biomech. Eng.* **142**, 121006. doi:10.1115/1.4047663

Sane, S. P. (2003). The aerodynamics of insect flight. *J. Exp. Biol.* **206**, 4191-4208. doi:10.1242/jeb.00663

Sane, S. P. (2016). Neurobiology and biomechanics of flight in miniature insects. *Curr. Opin. Neurobiol.* **41**, 158-166. doi:10.1016/j.conb.2016.09.008

Santhanakrishnan, A., Robinson, A. K., Jones, S., Low, A. A., Gadi, S., Hedrick, T. L. and Miller, L. A. (2014). Clap and fling mechanism with interacting porous wings in tiny insects. *J. Exp. Biol.* **217**, 3898-3909. doi:10.1242/jeb.084897

Santhanakrishnan, A., Jones, S. K., Dickson, W. B., Peek, M., Kasoju, V. T., Dickinson, M. H. and Miller, L. A. (2018). Flow structure and force generation on flapping wings at low reynolds numbers relevant to the flight of tiny insects. *Fluids* **3**, 45. doi:10.3390/fluids3030045

Schneider, C. A., Rasband, W. S. and Eliceiri, K. W. (2012). NIH Image to ImageJ: 25 years of image analysis. *Nat. Methods* **9**, 671-675. doi:10.1038/nmeth.2089

Spedding, G. R. and Maxworthy, T. (1986). The generation of circulation and lift in a rigid two-dimensional fling. *J. Fluid Mech.* **165**, 247-272. doi:10.1017/S0022112086003087

Sunada, S., Takashima, H., Hattori, T., Yasuda, K. and Kawachi, K. (2002). Fluid-dynamic characteristics of a bristled wing. *J. Exp. Biol.* **205**, 2737-2744. doi:10.1242/jeb.205.17.2737

Symonds, M. R. E. (2002). The effects of topological inaccuracy in evolutionary trees on the phylogenetic comparative method of independent contrasts. *Syst. Biol.* **51**, 541-553. doi:10.1080/10635150290069977

Taylor, G. K. and Thomas, A. L. R. (2014). *Evolutionary Biomechanics*. Oxford: Oxford University Press.

Ullman, D. E., Meideros, R., Campbell, L. R., Whitfield, A. E., Sherwood, J. L. and German, T. L. (2002). Thrips as vectors of tospoviruses. *Adv. Bot. Res.* **36**, 113-140. doi:10.1016/S0065-2296(02)36061-0

Usherwood, J. R. and Ellington, C. P. (2002). The aerodynamics of revolving wings. II. Propeller force coefficients from mayfly to quail. *J. Exp. Biol.* **205**, 1565-1576. doi:10.1242/jeb.205.11.1565

Voje, K. L. and Hansen, T. F. (2013). Evolution of static allometries: adaptive change in allometric slopes of eye span in stalk-eyed flies. *Evolution* **67**, 453-467. doi:10.1111/j.1558-5646.2012.01777.x

Wang, Z. and Tong, X. (2016). *Siamothrips balteus*, a new species of *Scirtothrips* genus-group from China (Thysanoptera, Thripidae). *Zookeys* **637**, 129-133. doi:10.3897/zookeys.637.10910

Weis-Fogh, T. (1973). Quick estimates of flight fitness in hovering animals, including novel mechanisms for lift production. *J. Exp. Biol.* **59**, 169-230. doi:10.1242/jeb.59.1.169

Weis-Fogh, T. (1975). Unusual mechanisms for the generation of lift in flying animals. *Sci. Am.* **233**, 80-87. doi:10.1038/scientificamerican1175-80

Zamar, M. I., Hernandez, M. C., Soto-Rodriguez, G. A. and Retana-Salazar, A. P. (2013). A new neotropical species of *Liothrips* (Thysanoptera: Phlaeothripidae) associated with *Ludwigia* (Myrtales: Onagraceae). *Rev. Soc. Entomol. Argentina* **72**, 83-89.

Zhang, H., Mound, L. A. and Xie, Y. (2010). A new genus and species from Southwestern China in the *Frankliniella* genus-group (Thysanoptera: Thripidae). *Zootaxa* **2729**, 65-68. doi:10.11646/zootaxa.2729.1.6

SUPPLEMENTARY MATERIALS AND METHODS

Forewing morphology images

We required that each published forewing image considered for measurements met the following criteria: 1) contained a scale bar; 2) consisted of least one forewing zoomed out with all bristles shown; and 3) had no noticeable damage to any of the forewing bristles. For thrips, we used a different set of images for measurements of G and D, as we needed to substantially magnify each of these images (as compared to measurements of S_{max}, A_T and n). We required that the published forewing images considered for G and D measurements had a spatial resolution of at least 6 pixels per bristle diameter, similar to the criterion used by Jones et al. (2016). As G and D measurements were used to compute non-dimensional G/D ratios, we did not restrict the images selected for G and D measurements to only those that contained a scale bar (i.e. measurements of G and D in pixels sufficed to calculate the dimensionless G/D ratio). However, this resulted in mutually exclusive datasets in thrips for G/D versus the other variables (Appendix S1). We also note that we were unable to ensure bristle position or angle was unaffected during imaging. Thus, while we ensured that there was no visual damage to bristles, it is possible that the measurements of G were somewhat affected by the positioning uncertainty. High-magnification images of free-flying tiny insect wings are needed to address these two measurement uncertainties. Regardless, we expect this effect to be minor, as we measured G at the bristle root, where it attaches to the solid membrane. Rotation should be minimized at this location.

Phylogeny simulation details

We simulated phylogenies for our study taxa because very few of our study species have been sampled in published phylogenies. Of our 38 species of thrips with phenotypic data, only eight were in any one of the most comprehensive phylogenies published to date (Buckman et al., 2013; Lima and Mound, 2016; Pereyra et al., 2019). For fairyflies, the most comprehensive species-level phylogeny included only one of our 21 species (Munro et al., 2011). Moreover, no tree was ultrametric (i.e. all branches of extant species contemporaneous), which is optimal for phylogenetic comparative analyses (Butler and King, 2004; O'Meara, 2012). Thus, because most of our species could not be placed in phylogenies, we simulated many possible phylogenies for our study species and conducted regressions across these trees. This procedure allowed for both integration over phylogenetic uncertainty (Martins, 1996) and for assessment of the sensitivity of our results to any specific potential phylogeny (Losos, 1994). Moreover, we note that our regression analyses are likely to be robust to phylogenetic variation or inaccuracy for many reasons. First, the phylogenetic regression is generally robust to tree misspecification (Stone, 2011). Second, our use of lambda

should mitigate problems associated with contrasting phylogenetic and phenotypic structure in our data (e.g. phenotypically very different but closely related species, as in the same genus; Martins and Housworth 2002). Finally, ordinary least-squares regression (i.e. without phylogeny) and phylogenetic regression both give unbiased estimates of the interspecific regression slope (Pagel, 1993; Rohlf, 2006), our focus here.

Adding some phylogenetic structure to simulated trees, rather than using completely random approaches, increases accuracy in downstream comparative analyses (Housworth and Martins, 2001; Martins, 1996; Martins and Housworth, 2002; Symonds, 2002). Thus, we ensured the simulated trees fit best estimates of taxonomy, given that taxonomy in principle reflects estimates of evolutionary relationships. At the lowest taxonomic level, all species of given genus were each other's closest relatives in every simulated tree. By adding additional taxonomic structure (i.e. subfamilies, families, suborders), our simulated trees were similarly constrained to best represent estimated relationships among higher taxa (Buckman et al., 2013).

For thrips, we first extracted taxonomic information from the Thrips Wiki (https://thrips.info/wiki/; accessed 15 March 2021). This source is updated regularly by researchers studying thrips systematics and is consistent with the current best estimate of higher-level thrips phylogeny (Buckman et al., 2013). Data were extracted on genera within families and families within the two major sub-orders of thrips (Terebrantia and Tubulifera). In some cases genera were placed into subfamilies, which were placed in families. All genera were included, including extinct genera and those unrepresented in our phenotypic data, to best simulate the branch-length structure among groups (e.g. mean genus age in a family of 100 genera will be lower than mean genus age in an equally old family of two genera). Current estimates of wasp systematics suggest that fairyflies are a polyphyletic group of two families in two superfamilies of wasps (Mymarommatoidea: Mymarommatidae and Chalcidoidea: Myrmaridae; Huber 1986; Davis et al. 2010; Munro et al. 2011). However, the two superfamilies may be sister clades, and Mymaridae is the sister family to all other clades within Chalcidoidea (Heraty et al., 2013; Munro et al., 2011). Thus, additional taxonomic structure would not have greatly improved our simulated trees. So for analysis purposes, we assumed these two families to be each other's sister taxon. We compiled genera for these two families from taxonomic accounts (Gibson et al., 2007; Huber, 2005, 2017; Lin et al., 2007; Poinar and Huber, 2011).

We simulated phylogenies in the package *phytools* v.0.7-70 (Revell, 2012) in R v.4.0.2 (R Core Team 2020). Because thrips and fairyflies are so distantly related phylogenetically (separated for more than 350 million years; Johnson et al., 2018; Misof et al., 2014), we started each simulated tree with these two groups as sister clades using the function "pbsim". We then simulated structure at sequentially lower taxonomic levels using the function "genus.to.species". These two functions simulated both tree topology and branch lengths. For both fairyflies and thrips, multiple levels of taxonomic ranks were imposed in simulations. In thrips, this meant randomly placing the branching time of the two suborders within Thysanoptera, then families within those suborders, subfamilies within some families, genera within (sub)families, and species within genera. For fairyflies, families were placed within superfamilies, genera within families, and species within genera.

We simulated 10,000 trees for our analyses. To remove variation in tree length due to stochastic simulation variation (Stadler, 2011), each simulated tree was rescaled to a total length of 1.0. Note that the relative (not absolute) amount of shared history between any two species determines the effect of phylogeny in PGLS (Hansen and Martins, 1996; Martins and Hansen, 1997). Thus our choice of 1.0 for tree length was arbitrary and did not affect our results. After simulation, each tree was pruned to only include the species for which we had phenotypic data, which varied based on the response variable (see above). We provide all tree simulation R code, taxonomic information, and resulting trees in Figshare as Appendices S2–4.

Bristled wing fabrication

The 3 mm thick solid membrane used in all the wing models were 3D printed with polylactic acid (PLA) filament using Craftbot printers (CraftUnique LLC, Stillwater, OK, USA). The bristles were made of type 304 stainless steel wires of varying diameter (Table S1), glued on top of the membrane. For flow-visualization measurements using particle image velocimetry (PIV), we made new wing models with the solid membrane laser cut from 3 mm thick acrylic sheets. Also, to avoid reflection in PIV measurements, the bristles were blackened using a blackener kit (Insta-Blak SS-370, Electrochemical Products, Inc., New Berlin, WI, USA).

Dynamically scaled robotic platform

Bristled wing models were attached to 6.35 mm diameter stainless steel D-shafts via custom aluminum L-brackets. Two 2-phase hybrid stepper motors with integrated encoders (ST234E, National Instruments Corporation, Austin, TX, USA) were used on each wing to perform rotation and translation. Rotational motion on a wing was achieved using a bevel gear for coupling a motor to a D-shaft. Translational motion was achieved using a rack and pinion mechanism driven by a second

motor. All four stepper motors (for a wing pair) were controlled using a multi-axis controller (PCI-7350, National Instruments Corporation, Austin, TX, USA) via custom programs written in LabVIEW software (National Instruments Corporation, Austin, TX, USA). The assembly was mounted on an acrylic tank measuring 0.51 m x 0.51 m in cross-section, and 0.41 m in height. The tank was filled to 0.31 m in height with a 99% glycerin solution, such that the wings were completely immersed in the fluid medium. This solution allowed us to achieve fluid properties relevant to tiny insect flight at a robot size large enough to accurately adjust the relevant parameters (see the **Test conditions** subsection in the main article).

Justification of forewing approach

Many miniaturized tiny insects possess hindwings as well as forewings (Jones et al., 2016, Santhanakrishnan et al., 2014, Kasoju et al., 2018, Cheng & Sun 2018, Lyu et al., 2019). From high-speed video recording of thrips (Santhanakrishnan et al., 2014, Cheng & Sun 2018, Lyu et al., 2019), it appears that there is a phase-lag between hind- and forewings during dorsal and ventral stroke reversal. As per our knowledge, wingbeat kinematics of hindwings of tiny insects have not been previously examined. In addition, a separate study would be required to understand the aerodynamic effects of including a phase lag between hind wings and fore wings. However, since these insects are flapping both hind wings and fore wings synchronously for most of the flapping cycle (except during dorsal and ventral stroke reversal), we expect that results for the forewing can be extended to the hindwing. Considering the above criteria, modelling just the forewing should be sufficient to understand the aerodynamic characteristics of bristled wing morphology. However, we recognize that this may be a fruitful area for future work.

Inter-wing spacing

The wing separation maintained in this study is similar to those observed in high-speed video recordings of free-flying thrips (Santhanakrishnan et al., 2014) and is also close enough to experience wing-wing interactions, but just far enough apart to prevent the leading and trailing edges of the rigid wing models from colliding during rotation. The variation in wing separation at the end of clap and start of fling is considered in our recent study (Kasoju and Santhanakrishnan, 2021), where we found that our smallest tested gap of 10% chord length between the wings augmented the aerodynamic force generation significantly. This occurred because the pressure distribution varied in the gap between the wings. Due to design limitations of our test facility, we were unable to test the case where the opposing wings come in full contact. More generally, if most species deviate the same way from our models, our results will apply equally to all of them. In other words, while our force measurements may underestimate the actual magnitudes, such an underestimation should

equally apply to all species, and thus our results on the effects of different variables (e.g. wingspan, bristle number, G, D) should be robust to this assumption.

Force measurements

A pause of 30 sec was introduced at the end of each run to remove the influence of wing-wake interaction occurring from the stroke reversal between runs. Another reason for introducing pause between runs is to remove any mechanical disturbance between runs (e.g. sudden bending of the L-bracket when the wings come to rest quickly). However, before commencing multiple runs for data collection (forces, TR-PIV, PL-PIV measurements), we operated the setup for at least 10 runs (without pausing between runs) to establish a periodic steady state in the tank. Operating for at least 10 runs before any data collection has been our standard protocol (Kasoju et al., 2018, Ford et al., 2019, Kasoju & Santhanakrishnan, 2021) to avoid any disturbances (such as sudden motion in a quiescent fluid) in data collection from the first run to the last run of data collection, and we favor it because this procedure helps us build a similar fluid environment for each run of data collection. In previous studies, this protocol was found to be helpful in maintaining repeatable force data collection between runs at high Reynolds number flows (Re_c>100). However, at a lower Reynolds number as in this study (Re_c=10), we did not see any noticeable difference from run to run with or without this protocol, since we were waiting for 30 seconds between run to run.

2D flow validation

Our assumption of 2D flow simplification is valid for two key reasons. First, in our previous study (Kasoju et al., 2018), we observed no flow along the z-direction of a rectangular bristled wing model. Second, in our more recent study (Kasoju & Santhanakrishnan, 2021), we found a very small region of non-zero 2D divergence in the flow field, suggesting that 2D flow simplification is a reasonable approximation. Our 2D flow simplification is also in agreement with a recent study (Santhanakrishnan et al., 2018) of a revolving elliptical wing of similar aspect ratio (~2) as this study, where spanwise flow was reduced for Re_c<10.

2D TR-PIV along wing chord

2D TR-PIV measurements were acquired for a total of 6 wing pairs, consisting of 2 wing pairs each for varying G, D and S. TR-PIV measurements were acquired along a chordwise (i.e. x-y) plane located at mid-span (Fig. 3A). The TR-PIV experimental setup and processing were similar to our previous studies (Kasoju et al., 2018; Ford et al., 2019) and are briefly summarized here. A single cavity Nd:YLF laser (Photonics Industries International, Inc., Bohemia, NY, USA) that provided a 0.5 mm diameter beam of 527 nm in wavelength was used in combination with a plano-concave cylindrical lens (focal length=-10 mm) to generate a thin laser sheet (thickness≈3-5 mm) positioned

at mid-span (HP in Fig. 3A) to illuminate the field of view (FOV). TR-PIV images were acquired using a high-speed complementary metal-oxide-semiconductor (CMOS) camera with a spatial resolution of 1280 x 800 pixels, maximum frame rate of 1630 frames/s, and pixel size of 20 x 20 microns (Phantom Miro 110, Vision Research Inc., Wayne, NJ, USA). This camera was fitted with a 60 mm lens (Nikon Micro Nikkor, Nikon Corporation, Tokyo, Japan). Hollow glass spheres of 10-micron diameter (110P8, LaVision GmbH, Göttingen, Germany) were used as seeding particles. A frame rate of 90 Hz was used to capture 100 evenly spaced images during both clap and fling phases. The raw images were processed using DaVis 8.3.0 software (LaVision GmbH, Göttingen, Germany) using one pass with an interrogation window of 64x64 pixels and two subsequent passes of 32x32 pixels window size.

2D PL-PIV along wingspan

The PL-PIV setup was similar to that used in Kasoju et al. (2018) and is briefly described here. Illumination was provided using a double-pulsed Nd:YAG laser (Gemini 200-15, New Wave Research, Fremont, CA) with a wavelength of 532 nm, maximum repetition rate of 15 Hz, and pulse width in the range of 3–5 ns. A 10 mm focal length cylindrical lens was used to generate a thin laser sheet (thickness≈3-5 mm) for illuminating the FOV. Raw PL-PIV images were acquired using a scientific CMOS (sCMOS) camera with a maximum spatial resolution of 2600 x 2200 pixels (maximum pixel size=6.5 x 6.5 microns) at a frame rate of 50 frames/s (LaVision Inc.,Ypsilanti, MI, USA), mounted with a 60 mm lens (same lens as in TR-PIV). The camera was focused on the seeding particles (same particles as in TR-PIV) along the laser sheet. PL-PIV measurements were acquired for all the wing models along 2 spanwise planes (VP1: fling and VP2: clap; see Fig. 3C) located at $0.5L_b$ measured from the membrane. Raw image pairs were acquired at 6 time points in clap and 7 time points in fling, with adjacent time points spaced by 6.25% τ. Laser pulse separation intervals between the 2 images of an image pair ranged from 1,500 -19,831 μs to obtain 6-8 pixels of particle displacement. The starting time point during the clap phase (τ=0.0625) was neglected due to very small changes in flow surrounding the wings. For each wing model tested, 5 image pairs were acquired at each time point for 5 continuous cycles of clap and fling. The raw image pairs were processed using DaVis 8.3.0 using one pass with an interrogation window of 64 x 64 pixels and two subsequent passes of 32 x 32 pixels window size. The processed PL-PIV images were phase-averaged over 5 cycles and the velocity field was exported to quantify the amount of fluid leaked through the bristles along the wingspan.

Circulation calculation

For a particular test condition (individually varying *G*, *D*, and *S*), the maximum absolute values of ω_z (i.e., $|\omega_z|$) at both LEV and TEV of a bristled wing were identified. Similar to Ford et al. (2019) and

Kasoju & Santhanakrishnan (2021), a 10%$|\omega_z|$ high-pass cut-off was next applied to isolate the vortex cores on a bristled wing model for that test condition. Γ of LEV or TEV was then calculated by selecting a region of interest (ROI) by drawing a box around a vortex core. A custom MATLAB script was used to automate the process of determining the ROI (Samaee et al. 2020). Essentially, we iterated the selection of ROI by starting with a small square box of 2 mm edge length and compared the Γ value with that of a bigger square box of 5 mm edge length. If the circulation values matched between the 2 boxes, then we stopped further iteration. If the circulation values did not match between the 2 boxes, we increased the size of the smaller box by 3 mm and repeated the process. In order to work with a single vortex (LEV or TEV) at a time and to remove any bias of Γ estimation, we ensured that ω_z of the oppositely signed vortex was zeroed out.Γ was determined for the right-hand wing only, with the assumption that circulation for the left wing was equivalent in magnitude but oppositely signed. Note that the left-wing motion is symmetric to the right wing about the *y-z* plane, making our assumption justifiable.

REFERENCES

Buckman, R. S., Mound, L. A. and Whiting, M. F. (2013). Phylogeny of thrips (Insecta: Thysanoptera) based on five molecular loci. *Syst. Entomol.* **38**, 123–133. doi:10.1111/j.1365-3113.2012.00650.x

Burnham, K. P. and Anderson, D. R. (2002). Model selection and multimodel inference: a practical information-theoretic approach. New York, NY: Springer-Verlag.

Butler, M. A. and King, A. A. (2004). Phylogenetic comparative analysis: a modeling approach for adaptive evolution. *Am. Nat.* **164**, 683–695. doi:10.1086/426002

Cheng, X., & Sun, M. (2018). Very small insects use novel wing flapping and drag principle to generate the weight-supporting vertical force. *J. Fluid Mech. 855*, 646-670. doi:10.1017/jfm.2018.668.

Davis, R. B., Baldauf, S. L. and Mayhew, P. J. (2010). The origins of species richness in the Hymenoptera: insights from a family-level supertree. *BMC Evol. Biol.* **10**, 109. http://www.biomedcentral.com/1471-2148/10/109.

Ford, M. P., Kasoju, V. T., Gaddam, M. G. and Santhanakrishnan, A. (2019). Aerodynamic effects of varying solid surface area of bristled wings performing clap and fling. *Bioinspir. Biomim.* **14**, 046003. doi:10.1088/1748-3190/ab1a00.

Gibson, G. A. P., Read, J. and Huber, J. T. (2007). Diversity, classification and higher relationships of Mymarommatoidea (Hymenoptera). *J. Hymenoptera Res.* **16**, 51–146.

Hansen, T. F. and Martins, E. P. (1996). Translating between microevolutionary process and macroevolutionary patterns: the correlation structure of interspecific data. *Evolution* **50**, 1404–1417.

Heraty, J. M., Burks, R. A., Cruaud, A., Gibson, G. A. P., Liljeblad, J., Munro, J., Rasplus, J. Y., Delvare, G., Jansta, P., Gumovsky, A. et al. (2013). A phylogenetic analysis of the megadiverse Chalcidoidea (Hymenoptera). *Cladistics* **29**, 466–542. doi:10.1111/cla.12006

Housworth, E. A. and Martins, E. P. (2001). Random sampling of constrained phylogenies: conducting phylogenetic analyses when the phylogeny is partially known. *Syst. Biol.* **50**, 628–639.

Huber, J. T. (1986). Systematics, biology, and hosts of the Mymaridae and Mymarommatidae (Insecta: Hymenoptera). *Entomography* **4**, 185–243.

Huber, J. T. (2005). The gender and derivation of genus-group names in Mymaridae and Mymarommatidae (Hymenoptera). *Acta Soc. Zool. Bohem.* **69**, 167–183.

Huber, J. T. (2017). *Eustochomorpha* Girault, *Neotriadomerus* gen. n., and *Proarescon* gen. n. (Hymenoptera, Mymaridae), early extant lineages in evolution of the family. *Journal of Hymenoptera Research* **57**, 1–87. doi:10.3897/jhr.57.12892

Johnson, K. P., Dietrich, C. H., Friedrich, F., Beutel, R. G., Wipfler, B., Peters, R. S., Allen, J. M., Petersen, M., Donath, A., Walden, K. K. O. et al. (2018). Phylogenomics and the evolution of hemipteroid insects. *Proc. Natl. Acad. Sci. USA* **115**, 12775–12780. doi:10.1073/pnas.1815820115

Jones, S. K., Yun, Y. J. J., Hedrick, T. L., Griffith, B. E. and Miller, L. A. (2016). Bristles reduce the force required to 'fling' wings apart in the smallest insects. *J. Exp. Biol.* **219**, 3759–3772. doi:10.1242/jeb.143362.

Kasoju, V. T., & Santhanakrishnan, A. (2021). Aerodynamic interaction of bristled wing pairs in fling. *Phys. Fluids*, *33*(3), 031901.

Kasoju, V. T., Terrill, C. L., Ford, M. P. and Santhanakrishnan, A. (2018). Leaky flow through simplified physical models of bristled wings of tiny insects during clap and fling. *Fluids* **3**, 44. doi:10.3390/fluids3020044.

Lima, É. F. B. and Mound, L. A. (2016). Systematic relationships of the Thripidae subfamily Sericothripinae (Insecta: Thysanoptera). *Zool. Anz.* **263**, 24–32. doi:10.1016/j.jcz.2016.03.001

Lin, N. Q., Huber, J. T. and LaSalle, J. (2007). The Australian genera of Mymaridae (Hymenoptera: Chalcidoidea). *Zootaxa* **1596**, 1–111. doi:10.11646/zootaxa.1596.1.1

Losos, J. B. (1994). An approach to the analysis of comparative data when a phylogeny is unavailable or incomplete. *Syst. Biol.* **43**, 117–123.

Lyu, Y. Z., Zhu, H. J., & Sun, M. (2019). Flapping-mode changes and aerodynamic mechanisms in miniature insects. *Physical Rev. E*, **99**(1-1), 012419. doi:10.1103/PhysRevE.99.012419.

Martins, E. P. (1996). Conducting phylogenetic comparative studies when the phylogeny is not known. *Evolution* **50**, 12–22.

Martins, E. P. and Hansen, T. F. (1997). Phylogenies and the comparative method: a general approach to incorporating phylogenetic information into the analysis of interspecific data. *Am. Nat.* **149**, 646–667.

Martins, E. P. and Housworth, E. A. (2002). Phylogeny shape and the phylogenetic comparative method. *Syst. Biol.* **51**, 873–880. doi:10.1080/10635150290155863

Misof, B. Liu, S. Meusemann, K. Peters, R. S. Donath, A. Mayer, C. Frandsen, P. B. Ware, J. Flouri, T. Beutel, R. G. et al. (2014). Phylogenomics resolves the timing and pattern of insect evolution. *Science* **346**, 763–767. doi:10.1126/science.1257570

Munro, J. B., Heraty, J. M., Burks, R. A., Hawks, D., Mottern, J., Cruaud, A., Rasplus, J. Y. and Jansta, P. (2011). A molecular phylogeny of the Chalcidoidea (Hymenoptera). *PLoS One* **6**, e27023. doi:10.1371/journal.pone.0027023

O'Meara, B. C. (2012). Evolutionary inferences from phylogenies: a review of methods. *Annu. Rev. Ecol. Evol. Syst.* **43**, 267–285. doi:10.1146/annurev-ecolsys-110411-160331

Pagel, M. (1993). Seeking the evolutionary regression coefficient: an analysis of what comparative methods measure. *J. Theoret. Biol.* **164**, 191-205.

Pereyra, V., Cavalleri, A., Szumik, C. and Weirauch, C. (2019). Phylogenetic analysis of the New World family Heterothripidae (Thysanoptera, Terebrantia) based on morphological and molecular evidence. *Insect Syst. Evol.* **50**, 702–716. doi:10.1163/1876312x-00002193

Poinar, G., Jr. and Huber, J. T. (2011). A new genus of fossil Mymaridae (Hymenoptera) from Cretaceous amber and key to Cretaceous mymarid genera. *Zookeys*, 461–472. doi:10.3897/zookeys.130.1241

R Core Team (2020). R: a language and environment for statistical computing. Vienna: R Foundation for Statistical Computing.

Revell, L. J. (2012). phytools: an R package for phylogenetic comparative biology (and other things). *Methods Ecol. Evol.* **3**, 217–223. doi:10.1111/j.2041-210X.2011.00169.x

Rohlf, F. J. (2006). A comment on phylogenetic correction. *Evolution* **60**, 1509–1515.

Samaee, M., Nelsen, N. H., Gaddam, M. G., & Santhanakrishnan, A. (2020). Diastolic vortex alterations with reducing left ventricular volume: an in vitro study. *J. Biomech. Eng.*, **142**(12), 121006. doi:10.1115/1.4047663.

Santhanakrishnan, A., Robinson, A. K., Jones, S., Low, A. A., Gadi, S., Hedrick, T. L. and Miller, L. A. (2014). Clap and fling mechanism with interacting porous wings in tiny insects. *J. Exp. Biol.* **217**, 3898–3909. doi:10.1242/jeb.084897.

Sokal, R. R. and Rohlf, F. J. (1995). *Biometry*. New York, NY: W.H. Freeman.

Stadler, T. (2011). Simulating trees with a fixed number of extant species. *Syst. Biol.* **60**, 676–684. doi:10.1093/sysbio/syr029

Stone, E. A. (2011). Why the phylogenetic regression appears robust to tree misspecification. *Syst. Biol.* **60**, 245–260. doi:10.1093/sysbio/syq098

Symonds, M. R. (2002). The effects of topological inaccuracy in evolutionary trees on the phylogenetic comparative method of independent contrasts. *Syst. Biol.* **51**, 541–553. doi:10.1080/10635150290069977
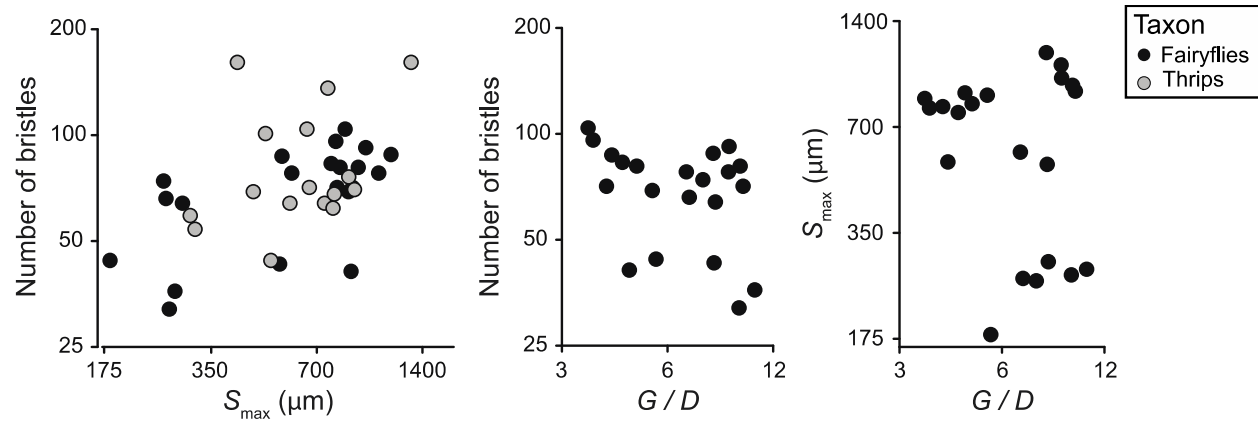
Fig. S1. Scatter plots of wing variables measured across thrips and fairyflies. All variables are plotted in raw units on a logged scale. Fairyfly data across all plots are from the same species. Thrips species measured for S_{max} and number of bristles (n) were different species than those for which we measured G/D, preventing plotting and correlation among those variables. All correlations among wing variables were low and statistically insignificant (Table S3).

Table S1. Experimental conditions and physical wing models used in this study. Each row represents the specific geometric variable or ratio that was controllably changed. Wing chord (c)=45 mm, membrane width (w)=7 mm, and bristle length (L_b)=19 mm were maintained constant across all wing models. G, D, S and n represent inter-bristle gap, bristle diameter, wingspan and number of bristles, respectively. 23 pairs of physical wing models were tested in this study. 3 wing pairs included in the case of varying n overlapped with 3 of the wing pairs considered in varying D, varying S and varying G/D conditions.

Experiment	Number of wing pairs tested	S [mm]	G [mm]	D [mm]	n	G/D
Changing G	4	81	1 – 2.1	0.2	70 – 132	5 – 10
Changing D	5	81	1.4	0.13 – 0.64	78 – 106	2 – 11
Changing S	5	67.5 – 94.5	1.3 – 1.8	0.25 – 0.36	88	5
Changing n	8	81	1 – 19	0.2 – 3.81	6 – 132	5
Changing G/D	4	81	1.2 – 1.8	0.15 – 0.6	88	2 – 11

Table S2. Results of regression model fitting of wing variables on body length in thrips and fairyflies. Models were fit separately for each variable. "Model" refers to parameter independence in thrips and fairyflies; the null model only contained a shared intercept and no slope, whereas the full model allowed a different slope and intercept for both groups. Each numerical value in the table is the mean across simulated phylogenies. AICc is the small-sample Akaike Information Criterion; low value indicates highest statistical support. w_i is the AICc weight, the probability that each model is the optimal model relative to the others (Burnham and Anderson 2002). Rank indicates the mean model rank across phylogenies, with 1 indicating the top model and 4 the poorest fit.

Model	Span (S_{max})			Bristle number			*G/D*		
	AICc	w_i	Rank	AICc	w_i	Rank	AICc	w_i	Rank
Null (same intercept, no slope)	50.95	0.000	4.000	33.93	0.001	4.000	46.26	0.000	4.000
Same slope + intercept	12.23	0.610	1.120	21.75	0.447	1.474	32.60	0.370	1.559
Same slope, different intercept	13.69	0.306	1.889	21.74	0.444	1.526	34.93	0.119	2.984
Full (slope + intercept different)	16.30	0.084	2.992	24.57	0.108	3.000	31.94	0.510	1.458

Table S3. PGLS correlations among wing variables. The correlation between S_{max} and n includes data from thrips and fairyflies. Correlations between S_{max} and G/D, as well as n and G/D, only included fairyflies, as thrips datasets for G/D versus n and S_{max} were mutually exclusive (Appendix S1). Correlations are on the lower diagonal (unshaded) and represent mean values across simulated phylogenies, corrected for bias (Rohlf 2006). *P*-values are on the upper diagonal (shaded) and likewise represent mean values across simulated phylogenies. *P*-values were calculated using Z-scores (Sokal and Rohlf, 1995).
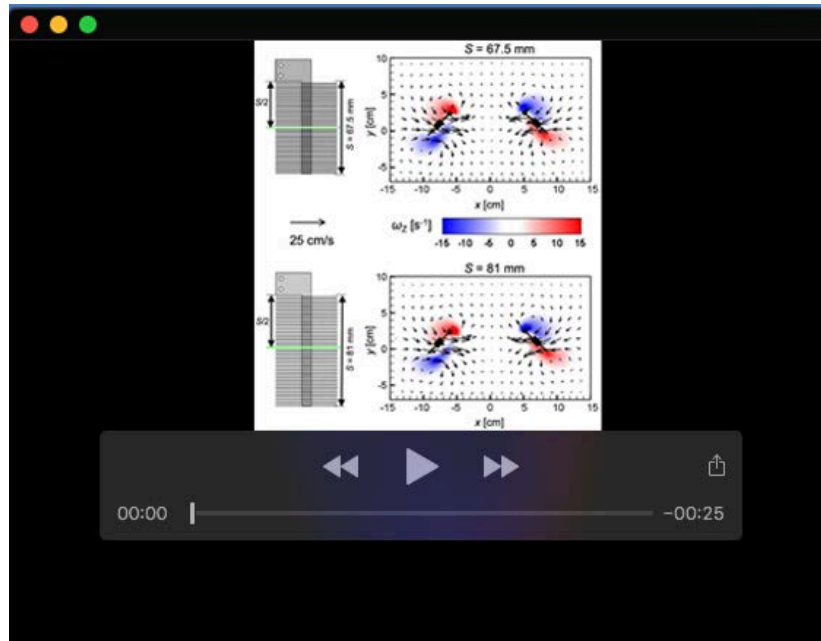
	S_{max}	n	G/D
S_{max}	-	0.078	0.211
n	0.431	-	0.133
G/D	-0.378	-0.511	-
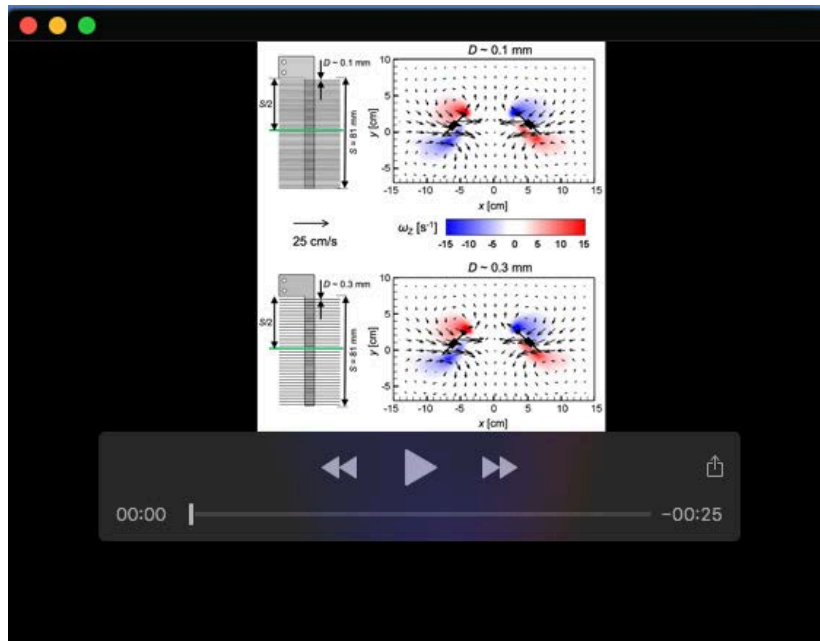
Movie 1. Velocity vectors overlaid on out-of-plane vorticity (ω_z) contours of bristled wing pairs during clap and fling, comparing the effect of increasing bristle diameter (D) from 0.1 mm to 0.3 mm. 10 equally spaced time instances are shown from start to end of clap, followed by 8 equally spaced time instances during fling.
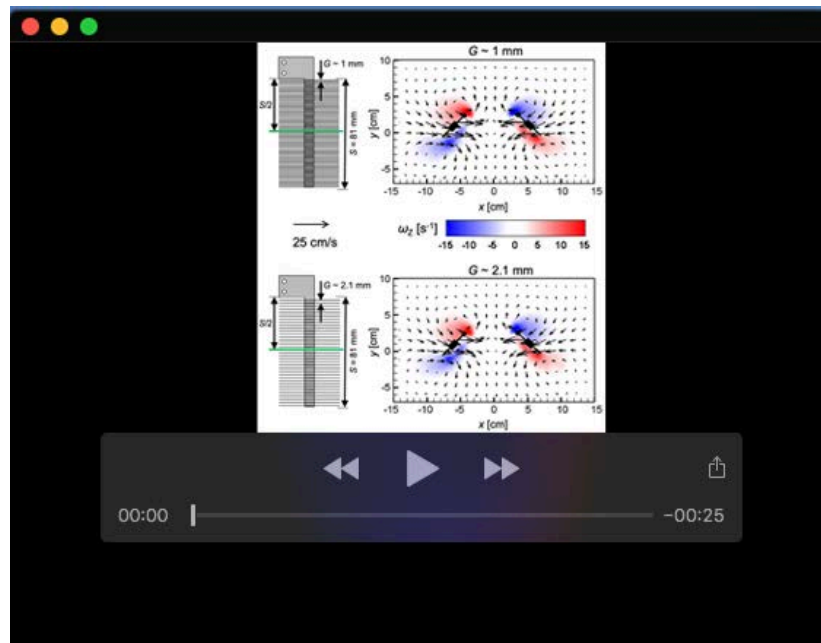
Movie 2. Velocity vectors overlaid on out-of-plane vorticity (ω_z) contours of bristled wing pairs during clap and fling, comparing the effect of increasing inter-bristle gap (*G*) from 1 mm to 2.1 mm. 10 equally spaced time instances are shown from start to end of clap, followed by 8 equally spaced time instances during fling.

Movie 3. Velocity vectors overlaid on out-of-plane vorticity (ω_z) contours of bristled wing pairs during clap and fling, comparing the effect of increasing wingspan (S) from 67.5 mm to 81 mm. 10 equally spaced time instances are shown from start to end of clap, followed by 8 equally spaced time instances during fling.